Direct Synthesis of Miniature Broadband Filters Using Hybrid BAW-Assisted Bridge-T Topologies for 5G Applications

Santi Cano, *Member, IEEE*, Eloi Guerrero, *Member, IEEE*, Alfred Giménez, Lluis Acosta, Carlos Caballero, *Associate Member, IEEE*, Yazid Yusuf, Jordi Verdú, *Senior Member, IEEE*, and Pedro de Paco, *Senior Member, IEEE*

***Abstract*—The ladder network is widely considered to be the most effective topology for acoustic wave (AW) filters in wireless communication. It is composed of either surface AW (SAW) or bulk AW (BAW) resonators, which allow for device miniaturization, low insertion loss, and high selectivity. However, with the introduction of increasingly wider bands in new wireless communication standards, AW ladder filters face topological limitations, as they require an electromechanical coupling factor (k_t^2) of approximately twice their fractional bandwidth (FBW). Although the k_t^2 can be increased beyond 15% using material systems such as scandium-doped aluminum nitride (ScAlN) or LNOI/LTOI, this typically comes at the cost of reduced quality factor. In contrast, bridge-T (BT) topologies decouple the relationship between the k_t^2 and the FBW through the introduction of balanced parallel-connected branches, enabling solutions that require significantly lower k_t^2. This work presents the complete design methodology for four BT topologies that demonstrate excellent performance in broadband applications, including a lowpass filter (LPF), a highpass filter (HPF), an LPF–HPF cascade, and two bandpass filters (BPFs). Since wideband filters cannot be synthesized using narrowband techniques, a direct bandpass (DB) approach based on the coupling matrix (CM) is employed to achieve full control over the entire design procedure. For validation purposes, the four BAW-assisted filters are fabricated using Sc-doped AlN solidly mounted BAW resonators, achieving extremely wideband responses with FBWs of 33% and insertion loss below 1.5 dB across the entire passband. The total device area, including the die mounted on the laminate, is 3×2 mm^2.**

***Index Terms*—Acoustic-wave filters, bandpass filter (BPF), bridge-T (BT) topology, bulk acoustic wave (BAW) resonator, coupling matrix (CM), direct bandpass (DB) synthesis, highpass filter (HPF), lowpass filter (LPF), wideband filter.**

I. Introduction

IN THE last decades, acoustic wave (AW) filters have played a crucial role in addressing the demand for radio frequency (RF) filters in wireless communication systems, thanks to their miniaturization capabilities, high selectivity, low insertion loss, improved temperature stability and power handling, among others [1], [2]. These on-chip AW filters are typically implemented using high quality factor resonators based on either surface AW (SAW) or bulk AW (BAW) technologies. They are commonly implemented as stand-alone devices for single-band responses [3] or integrated into more complex networks, such as duplexers or multiplexers that are connected to a common antenna port to satisfy carrier aggregation (CA) requirements [4], [5] of RF front-end modules (RF-FEMs) [6], [7].

The most common network used in AW filters is the ladder topology, which consists of N AW resonators alternately arranged in series and shunt. Despite being an unbeatable network for narrowband filters, recent advancements in wireless communication standards, particularly 5G and Wi-Fi, have introduced new wideband frequency bands that hinder the design and implementation of ladder networks due to technological constraints in achieving higher electromechanical coupling factors (k_t^2). Each AW resonator places a finite Ω_{TZ} that is linked to the resonance frequency f_s of the shunt resonators and to the anti-resonance frequency f_p of the series resonators. The distance between these two frequencies is proportional to k_t^2, which strictly limits the achievable fractional bandwidth (FBW) when maintaining standard technologies [8]. Indeed, as a rule of thumb, AW ladder filters require a k_t^2 of approximately twice their FBW. Several material systems have been proposed to increase the achievable bandwidth of AW filters, such as the enlargement of k_t^2 by either using scandium-doped aluminum nitride (ScAlN) [9], [10], [11] or lithium niobate (LiNbO3) [12], [13] piezoelectric materials. However, the price to pay is a reduction in the quality factor or the usage of technologies that are not CMOS-compatible. Consequently, to maintain low k_t^2 and achieve competitive insertion loss in current broadband designs, designers are usually forced to place the Ω_{TZs} very close to the passband, which in turn degrades the out-of-band (OoB) rejection.

Another approach is to employ topologies that decouple f_s from Ω_{TZ}, allowing filter designs with a lower k_t^2 compared to ladder ones. For example, transversal [14], [15], and lattice [16] configurations have demonstrated the ability to break the aforementioned relationship between k_t^2 and FBW.

Received 11 May 2026; revised 30 June 2026 and 11 August 2026; accepted 14 August 2026. Date of publication 1 September 2026; date of current version 21 October 2026. This work was supported in part by the Agencia Estatal de Investigación (AEI)—Ministerio de Ciencia e Innovación under Project PID2024-159605OB-I00 and in part by the Departament d'Universitats i Recerca. *(Corresponding author: Santi Cano.)*

Santi Cano, Jordi Verdú, and Pedro de Paco are with the Department of Telecommunications and Systems Engineering, Universitat Autónoma de Barcelona, 08193 Barcelona, Spain (e-mail: santi.cano@uab.cat).

Eloi Guerrero, Alfred Giménez, Lluis Acosta, Carlos Caballero, and Yazid Yusuf are with Qorvo Inc., Greensboro, NC 27409 USA.

Digital Object Identifier 10.1109/TMTT.2026.3726143

© 2026 The Authors. This work is licensed under a Creative Commons Attribution 4.0 License.
For more information, see https://creativecommons.org/licenses/by/4.0/

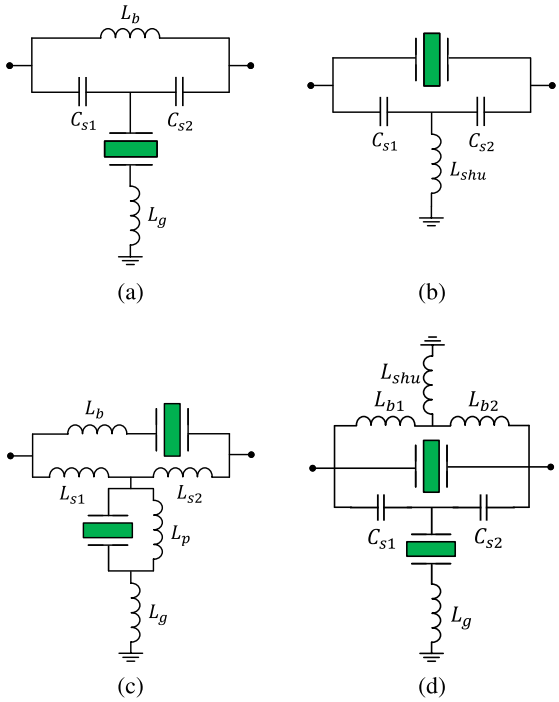


Fig. 1. Proposed BT topologies: (a) LPF, (b) HPF, (c) BPF 1, and (d) BPF 2.

Nevertheless, these topologies typically require a balun to compensate for the phase shift between the parallel-connected branches, limiting the operation range for wideband filters due to its poor electrical performance when it is manufactured. Another possible solution to avoid the appearance of a balun is to shift some reflection zeros to the complex plane, achieving the required phase shift to match both branches without relying on external elements [17], [18]. However, finding the complex reflection zero that provides the desired phase shift is quite challenging and often results in degraded OoB rejection. An alternative to transversal or lattice networks is the balanced bridge-T (BT) topology, where both pairs of arms have the same impedance. Mason [19] was one of the first to develop the set of transformations to convert a lattice into a BT, and use it in high-selectivity applications to improve the performance of telephone communications. Although his initial work with BT filters focused on planar designs, he also extended this concept to include piezoelectric crystals [20]. However, at that time the k_t^2 was lower than 1% for a quartz crystal. More recently, Yusuf [21], [22] proposed new BT networks exhibiting bandpass responses to enhance OoB rejection while improving the filter FBW, demonstrating that BT filters have found application in modern industry.

To the best of our knowledge, the synthesis of BT filters has not yet been addressed in the filter design community. This work proposes a general and scalable direct bandpass (DB) synthesis methodology for BT filters. Among all the networks proposed by Mason and Yusuf [19], [20], [21], [22], this work selects the BT topologies that offer the best performance for broadband filter design using modern BAW technology. Specifically, this work considers the four BT networks shown in Fig. 1. These hybrid BAW-assisted topologies include a lowpass filter (LPF), a highpass filter (HPF), and two bandpass filters (BPFs) that are implemented using reactive elements and Sc-doped AlN solidly mounted BAW resonators to ensure compact size and achieve low insertion loss. The synthesis procedure for obtaining the circuit elements of each BT is performed in the DB domain to avoid frequency-transformation errors that arise in wideband filter designs when using lowpass prototype approximations [23]. The element extraction is performed using the coupling matrix (CM) approach of [24], which operates in the DB domain. This approach is adopted because methods based on linear transformations are particularly useful for automatically identifying the additional elements required for network regularization. When this is not possible, they also allow the reformulation of the transfer function so that unnecessary elements are eliminated. In contrast, other extraction methods, such as the Darlington method [25], rely on prior knowledge of the existence and location of these elements within the topology. If they are not taken into account, inconsistencies between the transfer function and the realizable network prevent the synthesis procedure from converging to a valid solution.

Several proof-of-concept BAW-assisted designs are fabricated operating from 2.9 to 4.1 GHz, achieving an FBW of approximately 33.8% using BAW resonators with only $k_t^2 \approx 12.5\%$, instead of the $k_t^2 \approx 66\%$ that should be required by ladder topologies. Ladder filters alone are limited in their ability to realize extremely large FBWs, while BT topologies alone are not well suited to achieving high OoB rejection. However, by combining both approaches, it is possible to leverage the advantages of each topology and realize high-performance broadband filters.

To investigate effective strategies for combining different BAW-assisted cells, a prototype based on the combination of the LPF and HPF cells is fabricated and analyzed. This case study illustrates how additional elements may be introduced to regularize the network, how the CM can guide their optimal placement, and whether asymmetric solutions introduce practical limitations in AW technology. Although the presented LPF and HPF combination serves as a representative example, it is only one of many possible implementations. Alternative combinations of the proposed BT cells with ladder networks or more complex topologies may lead to even better performance. In this context, the design tools developed within the proposed methodology become especially valuable, since they enable the systematic exploration of multiple topological combinations until the most suitable solution is identified.

Finally, a sensitivity analysis is carried out to explain why BT topologies are significantly more sensitive than ladder networks and to identify the most critical elements when manufacturing tolerances are considered for mass production.

II. CM Nodal Interpretation

The classical CM model introduced by Atia et al. [26] can be related with the impedance matrix $\mathbf{Z}$ as [27]

$$\mathbf{Z} = \mathbf{G} + s\mathbf{W} + j\mathbf{M} \tag{1}$$

where $\mathbf{W}$ is the frequency matrix, $\mathbf{G}$ is the termination impedance matrix, and $\mathbf{M}$ is the CM that usually contains

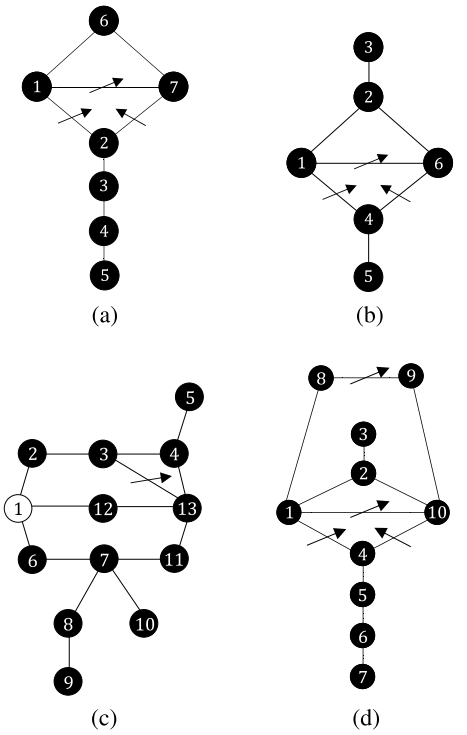


Fig. 2. Nodal representations of each BT topology: (a) LPF, (b) HPF, (c) BPF 1, and (d) BPF 2.

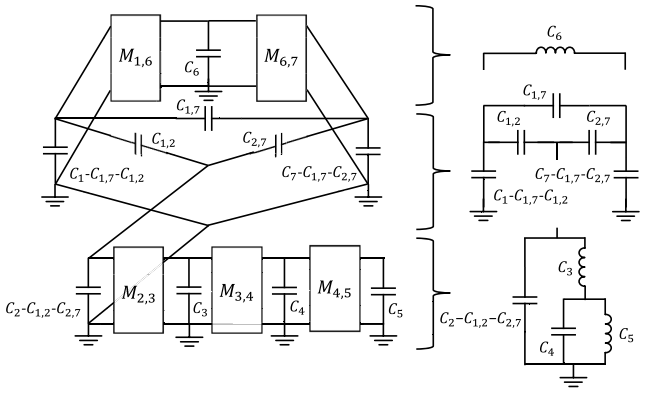


Fig. 3. Circuit interpretation of Fig. 2(a) before using the admittance inverters.

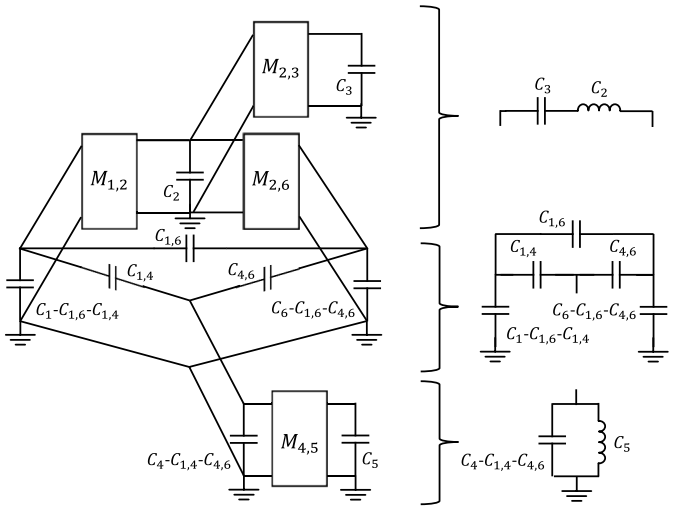


Fig. 4. Circuit interpretation of Fig. 2(b) before using the admittance inverters.

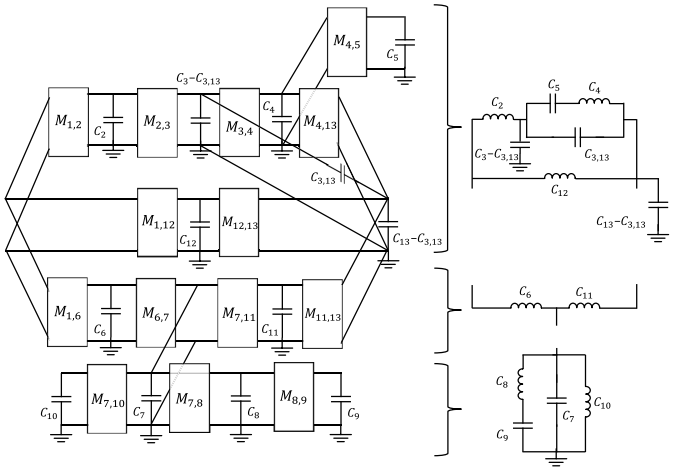
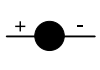
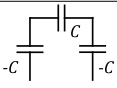
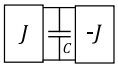


Fig. 5. Circuit interpretation of Fig. 2(c) before using the admittance inverters.

TABLE I

RELATIONSHIP BETWEEN CIRCUIT AND NODAL REPRESENTATIONS OF THE FOUR MAIN REACTIVE ELEMENT CONFIGURATIONS

	Shunt Capacitor	Series Capacitor	Shunt Inductor	Series Inductor
Nodal Representation				
Circuit Representation				

all the frequency-invariant couplings and frequency-invariant reactances (FIRs).

However, frequency-invariant elements tend to degrade wideband filtering responses. Since the goal of this work is to realize extremely wideband filters, the interpretation proposed in [24] is particularly advantageous, as it represents the network exclusively through reactive nodes. As explained in [24], all couplings inside the CM are normalized to unity so that they act as admittance inverters, allowing the frequency matrix **W** to directly identify all frequency-dependent elements to be extracted. In this way, the four main reactive element configurations and their equivalent nodal representations are summarized in Table I: shunt capacitors correspond to single reactive nodes, series capacitors appear as π-type frequency-variant couplings (FVCs) [28], shunt inductors are represented as dangling nodes, and series inductors correspond to reactive nodes placed between admittance inverters of different sign. From these four main configurations, more complex topologies can be derived. Fig. 2 illustrates the corresponding CM nodal representations of the BT topologies shown in Fig. 1. For clarity, Figs. 3–6 present equivalent diagrams of Fig. 2(a)–(d), respectively, to provide a clearer understanding of the proposed nodal descriptions.

Some BT topologies include additional shunt capacitors that are not shown in Fig. 1, nor considered in the proposals

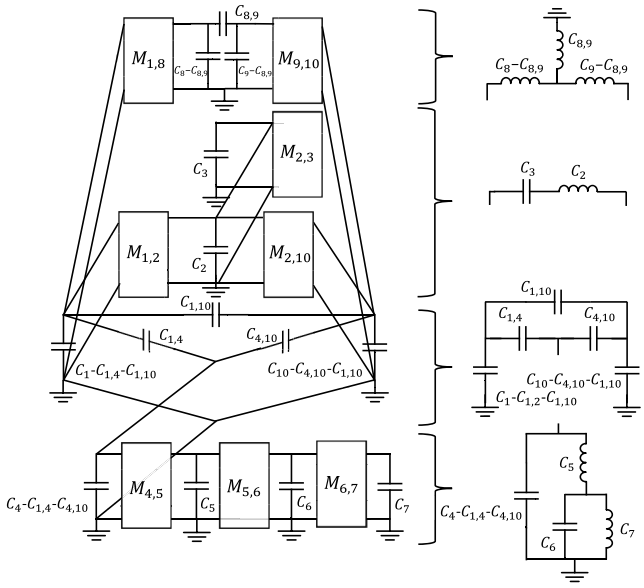


Fig. 6. Circuit interpretation of Fig. 2(d) before using the admittance inverters.

of Mason or Yazid [19], [20], [21], [22], since their analyses are restricted to symmetric cases. In contrast, the CM interpretation presented in [24] enables the identification of additional elements that arise in more general or asymmetric configurations, which are required to regularize the network. For example, even if symmetry is assumed in the LPF topology of Fig. 3, the shunt capacitors at nodes 1, 2, and 7 can only be eliminated if node 2 is scaled such that $C_2 = C_{1,2} + C_{2,7}$. In any other possible scaling, the shunt capacitors at nodes 1, 2, and 7 must remain. The same situation occurs in the HPF and BPF 2 topologies. Another different example is the BPF 1 topology shown in Fig. 5, where node 12 is not accounted for in Yazid's work. Omitting this node causes the missing element to manifest as cross couplings in the CM. If these couplings are neglected, the expected BT response may be degraded a lot. Let us highlight that node 1 in Fig. 2(c) is a blank node that does not contain any circuit element. It is introduced to allow the capacitors inside nodes 2 and 6 to be transformed into inductors.

Once the nodal representation is associated with each network, the first step consists of defining the filtering function and computing the transversal CM. The S-parameters of a filter in the normalized domain $s = \Sigma + j\Omega$ are defined in terms of the characteristic polynomials $P(s)$, $F(s)$, and $E(s)$ as [27]

$$\begin{bmatrix} S_{11}(s) & S_{12}(s) \\ S_{21}(s) & S_{22}(s) \end{bmatrix} = \frac{1}{E(s)} \begin{bmatrix} F(s)/\varepsilon_r & P(s)/\varepsilon \\ P(s)/\varepsilon & (-1)^N F(s)^*/\varepsilon_r \end{bmatrix} \tag{2}$$

where the roots of $P(s)$, $F(s)$, and $E(s)$ represent the Ω_{TZ}, reflection zeros (Ω_{RZ}), and poles of the filtering function, respectively, and ε_r and ε are the normalization constants that ensure monic polynomials. The HPF and BPF1 presented in Fig. 1 are not fully canonical networks, which means that the order of $F(s)$ is greater than that of $P(s)$, with the constants ε_r and ε defined as

$$\varepsilon = \frac{1}{\sqrt{10^{RL/10} - 1}} \left| \frac{P(\Omega)}{F(\Omega)} \right| \quad \varepsilon_r = 1. \tag{3}$$

Therefore, there is one or more Ω_{TZ} placed at ∞, making the OoB rejection decrease monotonically toward infinity. However, the LPF and BPF 2 in Fig. 1 are fully canonical networks because they require a polynomial $P(s)$ of higher order than $F(s)$, making it necessary to redefine the normalization constants as

$$\varepsilon = 1 \quad \varepsilon_r = \sqrt{10^{RL/10} - 1} \cdot \left| \frac{F(\Omega)}{P(\Omega)} \right|. \tag{4}$$

This implies that all Ω_{TZ} are finite, and one or more Ω_{RZ} are now located at infinity. Consequently, the OoB rejection increases monotonically as the frequency approaches infinity.

The characteristic polynomials can be related to the admittance parameters as detailed in [27], which, according to (1), contain the information of the $\mathbf{M}$ and $\mathbf{W}$ matrices

$$\mathbf{Y} = \frac{1}{y_d(s)} \begin{bmatrix} y_{11n}(s) & y_{12n}(s) \\ y_{21n}(s) & y_{22n}(s). \end{bmatrix} \tag{5}$$

Expressing this admittance matrix in terms of its partial fraction expansion yields the following equation [27]:

$$\mathbf{Y} = \begin{bmatrix} K_{11} & K_{12} \\ K_{21} & K_{22} \end{bmatrix} + \sum_{k=1}^{N} \frac{1}{(s - j\lambda_k)} \begin{bmatrix} r_{11} & r_{12} \\ r_{21} & r_{22} \end{bmatrix} \tag{6}$$

where the constant terms $K_{11} = sW_{SS} + jM_{SS}$ and $K_{22} = sW_{LL} + jM_{LL}$ are the source and load elements of the $\mathbf{M}$ and $\mathbf{W}$ matrices, the poles λ_k correspond to the eigenvalues (EVs) of the $N + 2 \times N + 2$ CM, the residues $r_{12}/(r_{22})^{1/2} = M_{Lk}$ and $(r_{22})^{1/2} = M_{Sk}$ are the off-diagonal elements of the $N + 2 \times N + 2$ CM, and the diagonal of $\mathbf{W}$ is initially set to 1. It is important to emphasize that the EVs cannot be arranged arbitrarily. In order to serialize the series inductors, their reactive nodes must be associated with odd EVs so that the adjacent inverters maintain opposite signs after applying the set of similarity transformations to obtain the desired BT topology.

Once the transversal $\mathbf{M}$ and $\mathbf{W}$ matrices are obtained, a different set of similarity transformations is carried out to reach each of the nodal representations of Fig. 2. These similarity transformations or rotations [27] are carried out by premultiplying and postmultiplying $\mathbf{M}$ and $\mathbf{W}$ by a rotation matrix $\mathbf{R}$ and its transpose $\mathbf{R}^T$, such as

$$\mathbf{M}_1 = \mathbf{R}\mathbf{M}_0\mathbf{R}^T \tag{7}$$

$$\mathbf{W}_1 = \mathbf{R}\mathbf{W}_0\mathbf{R}^T \tag{8}$$

where $\mathbf{R}$ defines a rotation in the plane $[i, j]$ $(i \neq j)$ by θ radians. This matrix has all diagonal elements equal to 1 and all off-diagonal elements equal to 0, except for $\mathbf{R}(i,i) = \mathbf{R}(j,j) = \cos(\theta)$ and $\mathbf{R}(j,i) = -\mathbf{R}(i,j) = \sin(\theta)$. To annihilate a specific nonzero element of the CM, it is necessary to find a rotation angle θ_r such that

$$\theta_r = \tan^{-1}\left(\mathbf{M}_{i,k}/\mathbf{M}_{j,k}\right) \tag{9}$$

or equivalently for the $\mathbf{W}$ matrix

$$\theta_r = \tan^{-1}\left(\mathbf{W}_{i,k}/\mathbf{W}_{j,k}\right). \tag{10}$$

The angle in (9) will annihilate $\mathbf{M}_{i,k}$, whereas the angle in (10) will annihilate $\mathbf{W}_{i,k}$ after performing a rotation with

expressions (7) and (8). Similarly, an existent $\mathbf{M}_{i,k}$ or $\mathbf{W}_{i,k}$ can be split to create additional couplings by setting θ_r to an arbitrary value different from (9). As a result, after the rotation, all couplings initially connected to i are also connected to j, and vice versa.

Apart from the annihilation or generation of an arbitrary position of the $\mathbf{M}$ and $\mathbf{W}$ matrices, FVCs can be generated in $\mathbf{W}_{i,j}$ by annihilating at the same time the couplings $\mathbf{M}_{i,k1}$ and $\mathbf{M}_{j,k2}$. This operation is known as "multiple annihilation" [28], and consists of scaling the rows and columns of one of the pivots in both $\mathbf{M}_{ii}$ and $\mathbf{W}_{ii}$ with

$$\alpha = \sqrt{\frac{-M_{j,k1} \cdot M_{j,k2}}{M_{i,k1} \cdot M_{i,k2}}}. \tag{11}$$

Once both $\mathbf{M}$ and $\mathbf{W}$ matrices are scaled by (11), a rotation can be performed with (7)–(9), and both $\mathbf{M}_{i,k1}$ and $\mathbf{M}_{j,k2}$ are annihilated, while an FVC in $\mathbf{W}_{i,j}$ is generated.

Finally, two additional matrix operations, represented in Fig. 7(a) and (b), must be introduced: CM expansion and CM reduction. CM expansion involves adding extra source and/or load nodes, which do not affect the magnitude of the filter response but shifts 90° its input and output phases by introducing an extra inverter, as shown in Fig. 7(a). Note that this operation inverts the normalized terminations of $\mathbf{G}$ in the new source and load nodes. The CM expansion is particularly useful in the following situations.

1) When the number of reactive nodes in the CM is lower than the number of circuit elements required by the BT topology. Diagonalizing the topology with these extra nodes will result in a new set of EVs. However, if the CM is diagonalized, the polynomial $P(s)$ must be multiplied by j if only one additional node is added to account for the 90° phase shift in the filtering function. On the other hand, if two additional nodes are included, the polynomial $F(s)$ must be multiplied by -1 to account for the 180° phase shift.
2) When the source and load nodes need to be rotated without modifying the network terminations.

In contrast, CM reduction [24] involves removing the source and/or load nodes along with the inverters that connect them to the rest of the network. The CM reduction is particularly useful when the target BT topology has a source-to-load FVC, such as the LPF of Fig. 2(a) or the BPF 2 of Fig. 2(d). On the one hand, if only the load node has to be eliminated, all couplings that connect the load to the internal nodes must be annihilated, except for the coupling between the load and the second node, as shown in Step 1 of Fig. 7(b). On the other hand, if only the source node has to be eliminated, all couplings that connect the source to the internal nodes must be annihilated, except for the coupling between the source and the second node, as illustrated in Step 2 of Fig. 7(b). If both nodes must be eliminated, both procedures are applied. Then, the coupling between the source and node 2 is split to create new connections: one from the source to the penultimate node, and another from the load to the second node. Using these new couplings, perform a multiple annihilation to generate the source-to-load FVC. Finally, the source and load nodes

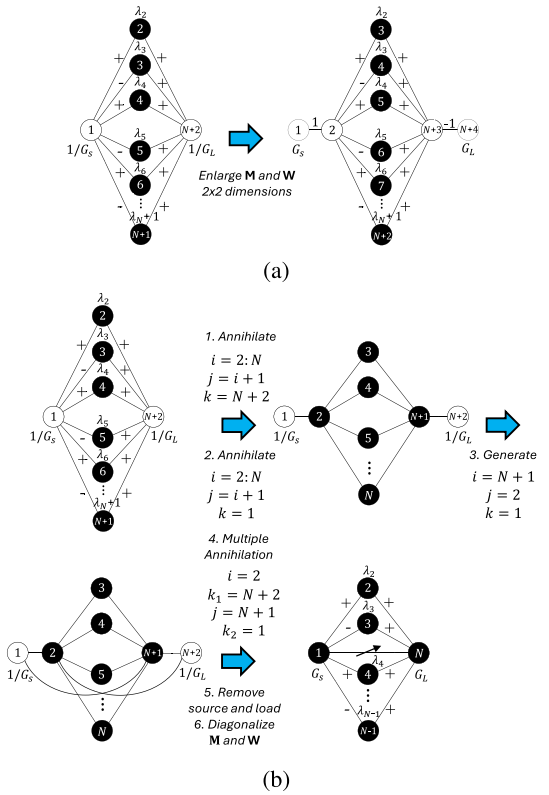


Fig. 7. Matrix operations: (a) matrix expansion and (b) matrix reduction.

are removed, which results in a 180° phase shift in the new CM. After diagonalization, the new transversal CM will yield a new set of EVs. This operation also inverts the terminations of G in the new source and load nodes.

When the network is a transversal CM, this operation introduces a source-to-load FVC, making reactive nodes the new source and load, as shown in Fig. 7(b). In this case, a set of similarity transformations is applied to remove all inverters M_{Sk} and M_{Lk} connected to the original source and load nodes and reassign them to the new reactive ones. Then, the M_{SN} and M_{LN} couplings are split, generating a M_{2N} coupling that is used to apply a multiple annihilation that generates the source-to-load FVC. Note that the normalized terminations of $\mathbf{G}$ are also inverted at the new source and load nodes. Moreover, it is necessary to diagonalize the $N \times N$ transversal CM to eliminate the internal couplings that have appeared throughout the entire process and are not depicted in Fig. 7(b) for clarity. Let us highlight that diagonalizing the transversal CM will yield a new set of EVs.

III. LPF and HPF Synthesis Methodology

In the case of the LPF in Fig. 1(a), a generalized Chebyshev filtering function [27] characterizes the passband within $\Omega = [-1, 1]$. Since the filtering function is designed to operate in the DB domain, the LPF response must exhibit symmetry about the origin. Consequently, the prescribed transmission zeros (Ω_{TZ}) must be specified in pairs of equal magnitude and opposite sign. Specifically, this LPF accommodates a fifth-order filtering function with 6 Ω_{TZ}: three Ω_{TZ} placed above

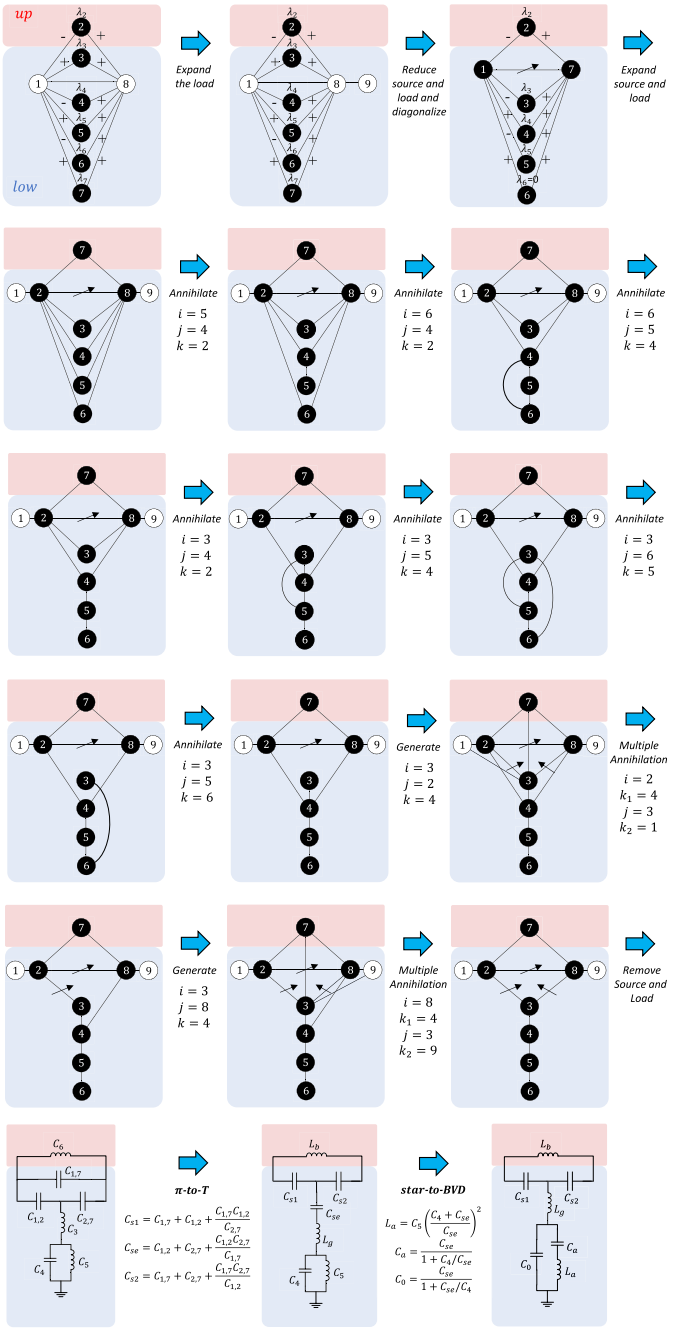


Fig. 8. Set of transformations to obtain the nodal representation of Fig. 2(a) from its transversal CM.

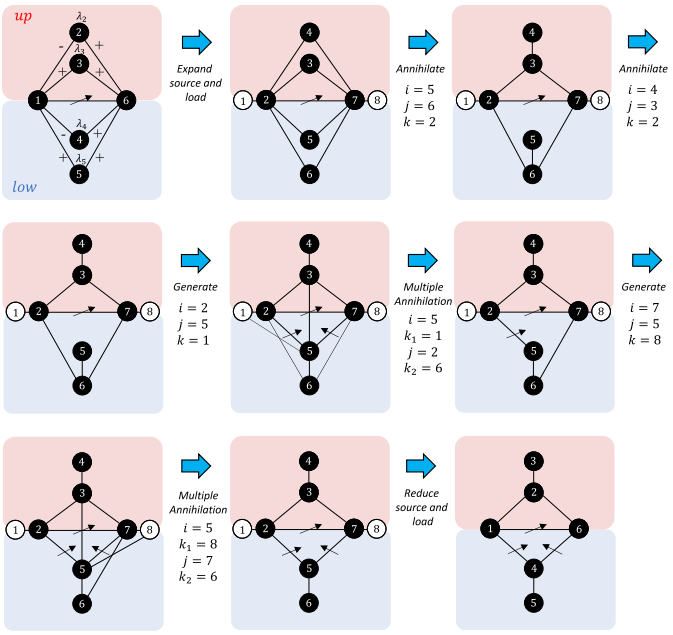


Fig. 9. Set of transformations to obtain the nodal representation of Fig. 2(b) from its transversal CM.

$\Omega = 1$ rad/s and their negative counterparts placed below $\Omega = -1$ rad/s. The order of the polynomial $P(s)$ is greater than $F(s)$ because the BVD resonator, together with inductor L_g, does not contribute a finite Ω_{RZ} but adds an extra Ω_{TZ} far from the band. This improves the OoB rejection before that Ω_{TZ} at the cost of degrading it as the frequency approaches infinity. For computing the corresponding characteristic polynomials, $P(s)$ is directly obtained from the prescribed Ω_{TZ}, whereas $F(s)$ is calculated using either the recursive technique of [27] or a Remez algorithm [29]. Since $P(s)$ is of higher order than $F(s)$, the ε and ε_r are calculated with (4).

The next step involves in calculating the transversal $\mathbf{M}$ and $\mathbf{W}$ matrices with (6), resulting in six reactive nodes. However, the circuit in Fig. 2(a) is composed by seven reactive nodes. An additional reactive node is included using the matrix expansion operation of Fig. 7(a) at the load of both $\mathbf{M}$ and $\mathbf{W}$ matrices. Notice that $P(s)$ had to be multiplied by j to compensate for the 90° phase shift introduced by the additional unitary inverter. Then, the matrix reduction operation is performed to create a source-to-load FVC. Since the load is already isolated, only the couplings connecting the source to the internal nodes are annihilated using Step 2 of Fig. 7(b). After diagonalizing $\mathbf{M}$ and $\mathbf{W}$, the rest of the similarity transformations to obtain the nodal representation of Fig. 2(a) are summarized in Fig. 8. Note that the additional shunt capacitors of nodes 1, 2, and 7 are neglected to reduce the number of reactive elements in the experimental validation of Section III-A. These capacitors are nullified through the cancellation produced by the negative shunt capacitances of the adjacent FVCs, provided that $S_{11} = S_{22}$ and nodes $M_{2,2}$ and $W_{2,2}$ are scaled by

$$\alpha_2 = \frac{W_{1,1} + W_{1,7}}{W_{1,2}}. \tag{12}$$

Finally, a lowpass-to-lowpass frequency transformation [27] is applied to scale the extracted elements to the upper cutoff frequency.

On the other hand, the HPF of Fig. 1(b) accommodates a generalized Chebyshev function of order $N = 5$ with 4 Ω_{TZ}: two finite Ω_{TZ} placed in the positive frequency plane and their mirrored Ω_{TZ} in the negative frequency plane. Unlike the LPF, the HPF inverts the characteristic polynomials $P(s)$ and $F(s)$ to achieve a highpass response when scaling the extracted elements with the lowpass-to-lowpass frequency transformation [27]. Therefore, the prescribed finite Ω_{TZ} becomes the Ω_{RZ},

$$\mathbf{M} = \begin{bmatrix} 0 & 0.1573 & -0.1573 & -0.8783 & -0.8783 & 1.1445 & 0 \\ 0.1573 & -0.9943 & 0 & 0 & 0 & 0 & 0.1573 \\ -0.1573 & 0 & 0.9943 & 0 & 0 & 0 & -0.1573 \\ -0.8783 & 0 & 0 & 2.0815 & 0 & 0 & -0.8783 \\ -0.8783 & 0 & 0 & 0 & -2.0815 & 0 & -0.8783 \\ 1.1445 & 0 & 0 & 0 & 0 & 0 & -1.1445 \\ 0 & 0.1573 & -0.1573 & -0.8783 & -0.8783 & -1.1445 & 0 \end{bmatrix}$$

(a)

$$\mathbf{W} = \begin{bmatrix} 1.2874 & 0 & 0 & 0 & 0 & 0 & -1.2874 \\ 0 & 1.0000 & 0 & 0 & 0 & 0 & 0 \\ 0 & 0 & 1.0000 & 0 & 0 & 0 & 0 \\ 0 & 0 & 0 & 1.0000 & 0 & 0 & 0 \\ 0 & 0 & 0 & 0 & 1.0000 & 0 & 0 \\ 0 & 0 & 0 & 0 & 0 & 1.0000 & 0 \\ -1.2874 & 0 & 0 & 0 & 0 & 0 & 1.2874 \end{bmatrix}$$

(b)

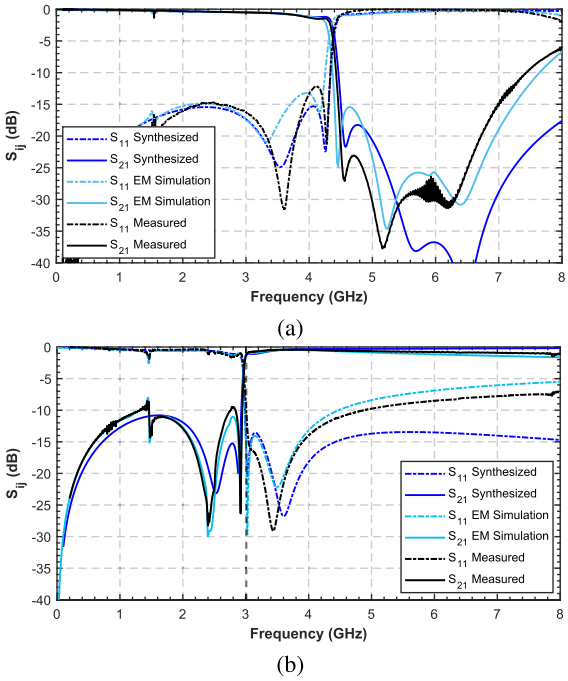
$$\mathbf{M} = \begin{bmatrix} 0 & 0 & 0 & 0 & 0 & -1.0000 & 0 \\ 0 & 0 & 1.0000 & 0 & 0 & 0 & 0 \\ 0 & 1.0000 & 0 & -1.0000 & 0 & 0 & 0 \\ 0 & 0 & -1.0000 & 0 & 1.0000 & 0 & 0 \\ 0 & 0 & 0 & 1.0000 & 0 & 0 & 0 \\ -1.0000 & 0 & 0 & 0 & 0 & 0 & 1.0000 \\ 0 & 0 & 0 & 0 & 0 & 1.0000 & 0 \end{bmatrix}$$

(c)

$$\mathbf{W} = \begin{bmatrix} 1.6935 & -0.8123 & 0 & 0 & 0 & 0 & -0.8812 \\ -0.8123 & 1.6246 & 0 & 0 & 0 & 0 & -0.8123 \\ 0 & 0 & 0.1570 & 0 & 0 & 0 & 0 \\ 0 & 0 & 0 & 20.6510 & 0 & 0 & 0 \\ 0 & 0 & 0 & 0 & 0.0443 & 0 & 0 \\ 0 & 0 & 0 & 0 & 0 & 0.7634 & 0 \\ -0.8812 & -0.8123 & 0 & 0 & 0 & 0 & 1.6935 \end{bmatrix}$$

(d)

Fig. 10. Matrices corresponding to the LPF of Fig. 2(a): (a) transversal **M** after matrix reduction, (b) transversal **W** after matrix reduction, (c) final **M**, and (d) final **W**.



(a) (b)

Fig. 11. S-Parameter filter responses of: (a) LPF and (b) HPF.

TABLE II
SYNTHESIZED ELEMENTS OF THE LPF AND HPF FILTERS

AW Parameters			
Resonator	C_{stat} **(pF)**	f_s **(MHz)**	k_t^2 **(%)**
LPF (SH)	1.755	4261	12.4
HPF (SE)	0.420	2900	12.7
LPF Lumped Elements			
C_{s1} (pF)	1.904	C_{s2} (pF)	1.904
L_b (nH)	1.411	L_g (nH)	0.290
HPF Lumped Elements			
C_{s1} (pF)	0.391	C_{s2} (nH)	0.391
L_{shunt} (nH)	3.732		

and the prescribed Chebyshev-like *RL* level is transformed to the equiripple OoB region. The set of transformations required to obtain the HPF topology is summarized in Fig. 9. Similar to the LPF, the additional shunt capacitors of nodes 1, 4, and 6 are neglected to reduce the number of reactive elements through the cancellation produced by the adjacent FVCs, provided that $S_{11} = S_{22}$ and nodes $M_{4,4}$ and $W_{4,4}$ are scaled by

$$\alpha_4 = \frac{W_{1,1} + W_{1,6}}{W_{1,4}}. \tag{13}$$

A. BAW-Assisted LPF and HPF Designs

To validate the synthesis methodology of both LPF and HPF, two BAW-assisted designs are carried out. In the case of the LPF, a fifth-order filter with $\Omega_{TZ} = [\pm 1.509, \pm 1.3026, \pm 1.062]$ rad/s, and $RL = 15.25$ dB is selected. After calculating the characteristic polynomials, the corresponding transversal **M** is obtained with (6). Fig. 10(a) and (b) illustrates the **M** and **W** matrices, respectively, once the matrix reduction operation is carried out. Then, the set of transformations summarized in Fig. 8 is applied, and all entries of **M** are scaled to 1, allowing the elements to be obtained directly from the nodal positions in **W**. The resulting **M** and **W** matrices are presented in Fig. 10(c) and (d), respectively. Table II lists the extracted elements from **W** after scaling them to the upper cutoff frequency (4.1 GHz). The resulting LPF response is depicted in Fig. 11(a). Let us highlight that all synthesized responses shown in this article correspond to the ideal Chebyshev filters after incorporating lossy inductors, capacitors, and mBVD resonator models. This is done to provide a closer representation of the EM simulated and measured responses.

In the case of the HPF, a fifth-order filter with $\Omega_{TZ} = [\pm 1.181, \pm 1.040]$ rad/s, and $RL = 14.57$ dB is selected. After calculating the characteristic polynomials, the transversal **M** and **W** matrices are represented in Fig. 12(a) and (b), respectively. Then, the set of transformations depicted in Fig. 9 is applied, and all entries of **M** are scaled to 1, allowing the elements to be obtained directly from the nodal positions in **W**. The resulting **M** and **W** matrices are presented in Fig. 12(c) and (d), respectively. Table II lists the extracted elements from **W** after scaling them to the lower cutoff frequency (2.9 GHz). The resulting HPF response is depicted in Fig. 11(b).

After extracting the circuit elements, the BAW resonators of both filters are co-simulated on a 750 × 525 μm die. The resonators are designed using the information provided by Table II: the areas are calculated using the static capacitances, while the k_t^2 values determine the material system to be employed. In this case, Sc-doped AlN solidly mounted BAW resonators are used. To simplify the trimming process during fabrication, only three distinct f_s are employed for all BT designs: 2900, 4030, and 4261 MHz. The border ring [30], [31] technique is employed in the HPF resonator to mitigate

$$\mathbf{M} = \begin{bmatrix} 0.0000 & -0.1377 & -0.1377 & 0.2994 & 0.2994 & -0.0000 \\ -0.1377 & -0.9901 & 0 & 0 & 0 & 0.1377 \\ -0.1377 & 0 & 0.9901 & 0 & 0 & 0.1377 \\ 0.2994 & 0 & 0 & 0.9881 & 0 & 0.2994 \\ 0.2994 & 0 & 0 & 0 & -0.9881 & 0.2994 \\ -0.0000 & 0.1377 & 0.1377 & 0.2994 & 0.2994 & 0.0000 \end{bmatrix}$$

(a)

$$\mathbf{W} = \begin{bmatrix} 0.5102 & 0 & 0 & 0 & 0 & -0.5102 \\ 0 & 1.0000 & 0 & 0 & 0 & 0 \\ 0 & 0 & 1.0000 & 0 & 0 & 0 \\ 0 & 0 & 0 & 1.0000 & 0 & 0 \\ 0 & 0 & 0 & 0 & 1.0000 & 0 \\ -0.5102 & 0 & 0 & 0 & 0 & 0.5102 \end{bmatrix}$$

(b)

$$\mathbf{M} = \begin{bmatrix} 0 & -1.0000 & 0 & 0 & 0 & 0 \\ -1.0000 & -0.0000 & 1.0000 & 0 & 0 & 1.0000 \\ 0 & 1.0000 & 0.0000 & 0 & 0 & 0.0000 \\ 0 & 0 & 0 & 0.0000 & 1.0000 & 0 \\ 0 & 0 & 0 & 1.0000 & -0.0000 & 0 \\ 0 & 1.0000 & 0.0000 & 0 & 0 & 0 \end{bmatrix}$$

(c)

$$\mathbf{W} = \begin{bmatrix} 0.6938 & 0 & 0 & -0.3672 & 0 & -0.3266 \\ 0 & 26.3813 & 0 & 0 & 0 & 0 \\ 0 & 0 & 0.0387 & 0 & 0 & 0 \\ -0.3672 & 0 & 0 & 0.7345 & 0 & -0.3672 \\ 0 & 0 & 0 & 0 & 1.3946 & 0 \\ -0.3266 & 0 & 0 & -0.3672 & 0 & 0.6938 \end{bmatrix}$$

(d)

Fig. 12. Matrices corresponding to the HPF of Fig. 2(b): (a) initial transversal **M**, (b) final **M**, and (c) final **W**.

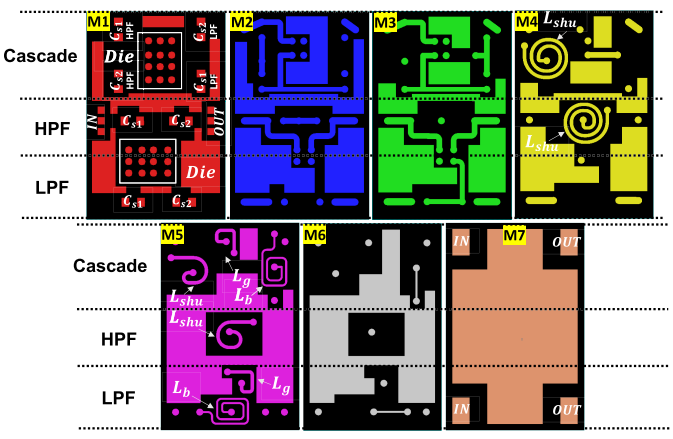
the impact of spurious lateral modes between f_s and f_p, which arise from Lamb waves that are not perfectly confined at the lateral boundaries of the resonators. Since this technique introduces undesired modes below f_s, it is not implemented in the LPF resonators to avoid notches in the passband.

The remaining reactive elements of both the LPF and HPF are implemented on a seven-layer laminate. Flip-chip technology is used to mount the dies on the laminate [32], [33]. The bumps of the flipped dies, together with the SMD capacitors C_{s1} and C_{s2} of the LPF and HPF, are placed on the top layer of the laminate. The intermediate layers contain the remaining inductors L_b and L_g of the LPF, as well as L_{shunt} of the HPF. The bottom layer acts as the ground plane. The laminate design is shown in Fig. 13(a), where the LPF is located at the bottom, the HPF in the middle, and the cascading of both filters at the top. The total device area, including two identical dies mounted on the laminate, is 3×2 mm. These dimensions are slightly larger than the actual footprint of a single BT topology, since three BAW-assisted filters are included in this set-up. Fig. 13(b) shows a top-view picture of the assembled design after flipping and mounting the dies onto the laminate.

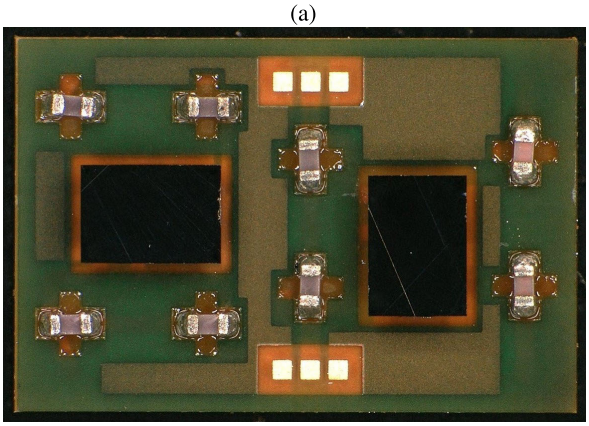
The LPF is measured using an evaluation board (EVB), whereas the HPF is measured with ground-signal-ground (GSG) probes. Fig. 11 compares the synthesized, simulated, and measured S-parameters of the two BAW-assisted filters. Let us highlight that all BAW-assisted filters in this work show a mirror mode at 1.5 GHz, caused by the Bragg reflector of the solidly mounted resonators.

IV. BPF Synthesis Methodology

In the case of the BPF 1 of Fig. 1(c), a reduced Chebyshev filtering function characterizes a dual-band response within



(a)



(b)

Fig. 13. 3×2 mm laminate containing the LPF, HPF, and their cascade: (a) 2-D design view and (b) top-view picture of the assembled design after flipping and mounting the dies onto the laminate.

$\Omega \in [-1, -f_{c1}/f_{c2}]$ and $\Omega \in [f_{c1}/f_{c2}, 1]$, using a Hermitian function that preserves the same information between the positive and negative frequency planes [34], [35]. Consequently, the prescribed transmission zeros (Ω_{TZ}) are specified in pairs of equal magnitude and opposite sign. For this reason, all the BPFs synthesized in the DB domain use a lowpass-to-lowpass frequency transformation [27] to scale the extracted elements to the upper cutoff frequency [23], [35].

The BPF of Fig. 1(c) accommodates a tenth-order filtering function with 9 Ω_{TZ}: one Ω_{TZ} at 0, two finite Ω_{TZ} placed above $\Omega = 1$ rad/s, two finite Ω_{TZ} placed below $\Omega = f_{c1}/f_{c2}$, and their mirrored counterparts in the negative frequency plane. In addition, there are also two imaginary reflection zeros ($j\Omega_{RZ}$) that model the values of L_g and L_b.

The next step involves in calculating the transversal **M** and **W** matrices with (6), resulting in eight reactive nodes. However, the circuit in Fig. 2(c) is composed by 11 reactive nodes. Two additional reactive nodes can be included using the matrix expansion operation of Fig. 7(a) at the source and load of both **M** and **W** matrices. Notice that $F(s)$ had to be multiplied by -1 to compensate for the 180° phase shift introduced by the additional unitary inverters. The remaining 11th reactive node is related to L_g. In fact, if node 12 of Fig. 14 is not included, the topology results in two symmetric cross-couplings between nodes 1 and 11, and between nodes 6 and

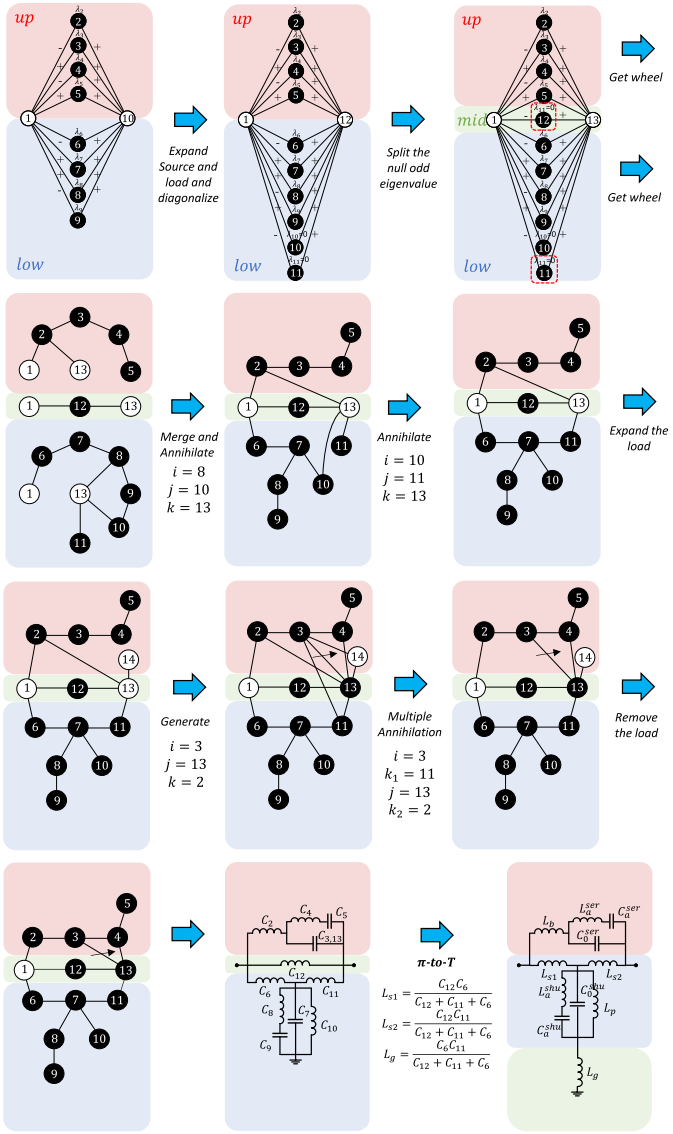


Fig. 14. Set of transformations to obtain the nodal representation of Fig. 2(c) from its transversal CM.

13 after applying the set of similarity transformations shown in Fig. 14. The magnitude of these cross-couplings depends on the allocation of the two $j\Omega_{RZ}$, and they become zero only in very specific cases, as shown in Fig. 15.

To avoid the appearance of the undesired cross-coupling, regardless of the $j\Omega_{RZ}$ value, it is necessary to increase the number of reactive nodes from 10 to 11 in the transversal CM with a specific condition. This is achieved by splitting the null odd EV into two parallel-connected nodes. The null odd EV is associated with the partial extraction at zero, and it is indicated as $\lambda = 0$ in Fig. 14. This node represents a series inductor that can be equivalently split into two parallel series inductors. First, let us express the lower branches of the admittance parameter $Y_{21}(s)$ of the transversal CM as shown in the following equation:

$$Y_{21}^{low}(s) = \frac{2M_{1,6}^2}{s-j\lambda_6} + \frac{2M_{1,6}^2}{s+j\lambda_6} + \frac{2M_{1,8}^2}{s-j\lambda_8} + \frac{2M_{1,8}^2}{s+j\lambda_8} + \frac{M_{1,10}^2 - M_{1,11}^2}{s} = \frac{s^4\left(2M_{1,6}^2+2M_{1,8}^2+M_{1,10}^2-M_{1,11}^2\right)+Y_{rem}(s)}{\left(s^2+\lambda_6^2\right)\left(s^2+\lambda_8^2\right)} \quad (14)$$

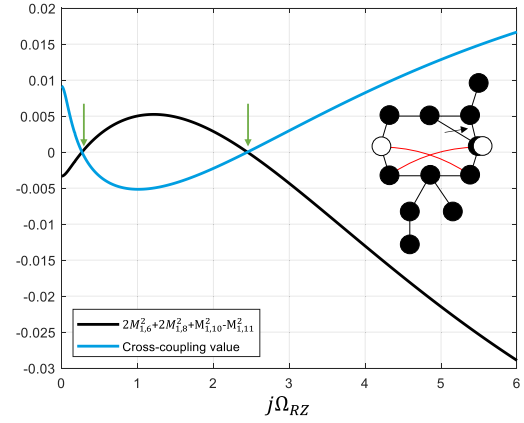


Fig. 15. Relationship between the cross-coupling, the pair of $j\Omega_{RZ}$ and the highest term of $Y_{21}^{low}(s)$.

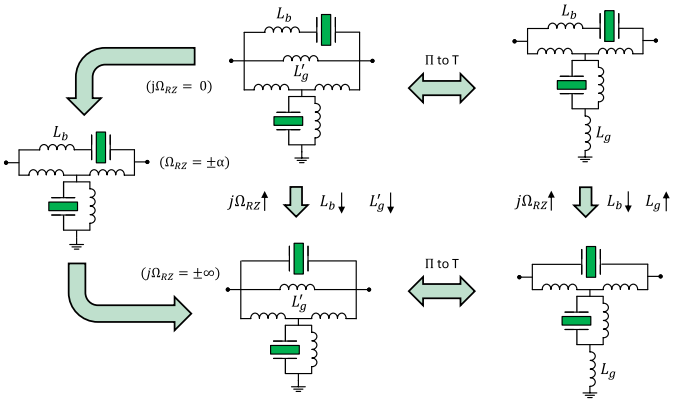


Fig. 16. Illustration of how different variants of the same topology are obtained when varying the allocation of the $\pm j\Omega_{RZ}$.

where $Y_{rem}(s)$ represents the remaining part of the admittance parameter that has not been mathematically expanded. By interpreting (14), the fourth-order term of the polynomial corresponds to the unwanted cross-coupling, as depicted in Fig. 15. When the leading coefficient is set to zero, the cross-coupling is annihilated. This can be achieved by splitting the null odd EV into two nodes. One of them cancels the highest order term by introducing a new coupling, given by

$$M_{1,12} = \sqrt{-\left(2M_{1,6}^2 + 2M_{1,8}^2 + M_{1,10}^2 - M_{1,11}^2\right)} \quad (15)$$

while the other coupling must satisfy the condition that, together with (15), their sum equals the original coupling

$$M_{1,11}^{new} = \sqrt{\left|M_{1,11}\right|^2 - M_{1,12}^2}. \quad (16)$$

Since the original node was a null EV, the two split nodes maintain their EV equal to 0. Once the split is done, the rest of the transformations necessary to obtain the BAW-assisted topology of Fig. 1(c) are represented in Fig. 14.

Interestingly, depending on the allocation of the $j\Omega_{RZ}$, different variants of the BPF 1 circuit can be obtained, as represented in Fig. 16, and all of them are considered by the proposed CM interpretation without loss of generality. When the $j\Omega_{RZ}$ tends to zero, the inductor L_b increases, whereas as $j\Omega_{RZ}$ tends to infinity, L_b vanishes. In contrast, when $j\Omega_{RZ}$ approaches a specific finite value, L_g disappears, which is

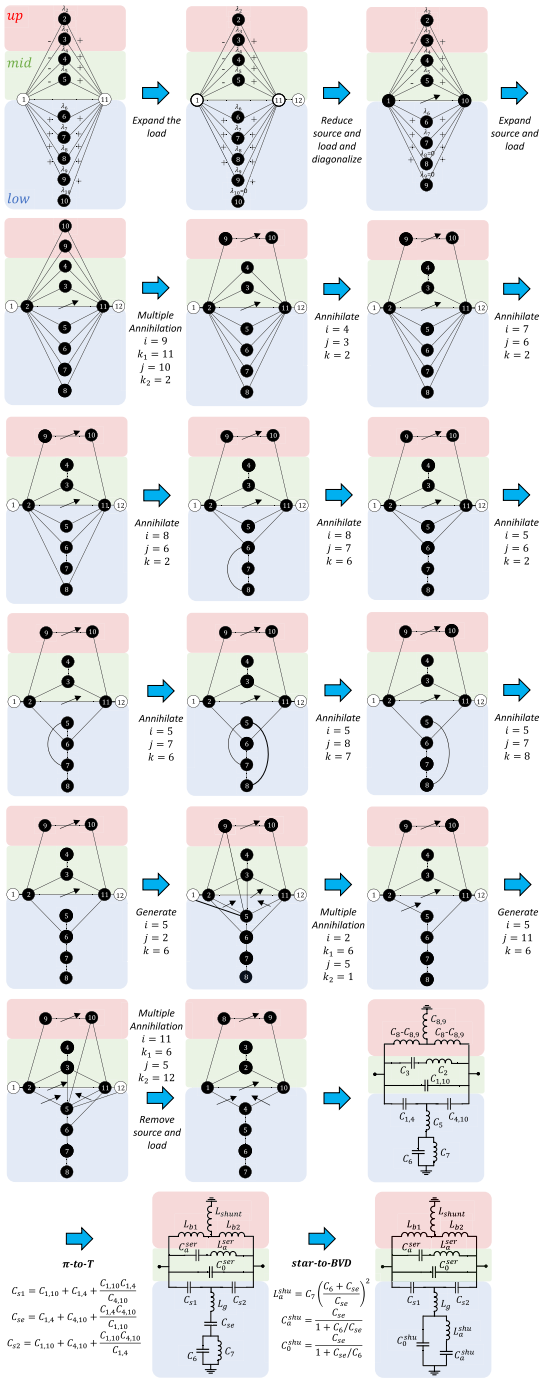


Fig. 17. Set of transformations to obtain the nodal representation of Fig. 2(d) from its transversal CM.

equivalent to the cross coupling becoming zero, as illustrated in Fig. 15.

On the other hand, the BPF 2 of Fig. 1(d) accommodates a generalized Chebyshev filtering function that characterizes a dual-band response within $\Omega \in [-1, -f_{c1}/f_{c2}]$ and $\Omega \in [f_{c1}/f_{c2}, 1]$ [35]. However, instead of being a tenth-order filtering function, this BPF is a eighth-order with 9 Ω_{TZ}: one Ω_{TZ} at 0, two finite Ω_{TZ} placed above $\Omega = 1$ rad/s, two finite Ω_{TZ} placed below $\Omega = f_{c1}/f_{c2}$, and their mirrored counterparts in the negative frequency plane. Similar to the LPF, this BPF has more TZs than RZs due to the contribution of the ground inductor beneath the shunt AW resonator. Therefore, the ε and ε_r are calculated with (4).

After calculating the characteristic polynomials, the transversal **M** and **W** matrices are calculated with (6), resulting in eight reactive nodes. However, the circuit in Fig. 2(d) is composed by nine reactive nodes. An additional reactive node is included using the matrix expansion operation of Fig. 7(a) at the load of both **M** and **W** matrices. Notice that $P(s)$ had to be multiplied by j to compensate for the 90° phase shift introduced by the additional unitary inverter. Then, the matrix reduction operation is performed to create a source-to-load FVC. Since the load is already isolated due to the previous matrix expansion operation, only the couplings connecting the source to the internal nodes are annihilated using Step 2 of Fig. 7(b). After diagonalizing **M** and **W**, the rest of the similarity transformations to obtain the nodal representation of Fig. 2(d) are summarized in Fig. 17. Note that the additional shunt capacitors of nodes 1, 4, and 10 are neglected to reduce the number of reactive elements in the experimental validation of Section IV-A. These capacitors are eliminated through the cancellation produced by the adjacent FVCs, provided that $S_{11} = S_{22}$ and nodes $M_{4,4}$ and $W_{4,4}$ are scaled by

$$\alpha_4 = \frac{W_{1,1} + W_{1,10}}{W_{1,4}}. \tag{17}$$

Let us highlight that a portion of the static capacitance of the series resonator can be redistributed and absorbed by the shunt resonator when performing the π-to-T and star-to-BVD transformations of Fig. 17. This arbitrary distribution allows for multiple technological solutions that yield the same filtering response. For instance, a case of interest is when the k_t^2 of both resonators is equal, as this allows them to be fabricated using the same material systems on a single die. To achieve this condition, both capacitance ratios r should be equated as

$$r_{ser} = r_{shu} \tag{18}$$

$$\frac{C_{1,10}\left(1 - \frac{1}{x}\right)}{C_a^{ser}} = \frac{C_6}{C_{1,4} + C_{4,10} + \frac{C_{1,4}C_{4,10}}{C_0^{ser}/x}} \tag{19}$$

where x is the portion of C_0^{ser} that must be redistributed to achieve $k_t^{2(ser)} = k_t^{2(shu)}$. By isolating x, a second-degree system of equations can be formulated to find the new capacitances C_{se} and C_0^{ser} that satisfy $k_t^{2(ser)} = k_t^{2(shu)}$, such that

$$C_{se} = \frac{C_0^{ser}}{x} \tag{20}$$

$$C_0^{ser} = C_{1,10}\left(1 - \frac{1}{x}\right). \tag{21}$$

A. BAW-Assisted BPF Designs

To validate the synthesis methodology of both BPFs, two BAW-assisted designs are developed. In the case of BPF 1, a tenth-order filter with $\Omega_{TZ} = [\pm 0.668, \pm 1.207, \pm 1.580, \pm 1.109, 0]$ rad/s, $j\Omega_{RZ} = \pm 4.448$ rad/s, and $RL = 35.22$ dB is selected. Considering that $f_{c1} = 2.95$ GHz and $f_{c2} = 4.1$ GHz,

$$\mathbf{M} = \begin{bmatrix}
0 & -0.3563 & -0.3563 & -2.1779 & -2.1779 & 0.1010 & -0.1010 & -0.3784 & 0.3784 & -0.5549 & 0.9376 & 0 \\
-0.3563 & 0.9721 & 0 & 0 & 0 & 0 & 0 & 0 & 0 & 0 & 0 & 0.3563 \\
-0.3563 & 0 & -0.9721 & 0 & 0 & 0 & 0 & 0 & 0 & 0 & 0 & 0.3563 \\
-2.1779 & 0 & 0 & 2.4778 & 0 & 0 & 0 & 0 & 0 & 0 & 0 & 2.1779 \\
-2.1779 & 0 & 0 & 0 & -2.4778 & 0 & 0 & 0 & 0 & 0 & 0 & 2.1779 \\
0.1010 & 0 & 0 & 0 & 0 & 0.6908 & 0 & 0 & 0 & 0 & 0 & 0.1010 \\
-0.1010 & 0 & 0 & 0 & 0 & 0 & -0.6908 & 0 & 0 & 0 & 0 & -0.1010 \\
-0.3784 & 0 & 0 & 0 & 0 & 0 & 0 & 1.3055 & 0 & 0 & 0 & -0.3784 \\
0.3784 & 0 & 0 & 0 & 0 & 0 & 0 & 0 & -1.3055 & 0 & 0 & 0.3784 \\
-0.5549 & 0 & 0 & 0 & 0 & 0 & 0 & 0 & 0 & 0 & 0 & -0.5549 \\
0.9376 & 0 & 0 & 0 & 0 & 0 & 0 & 0 & 0 & 0 & 0 & -0.9376 \\
0 & 0.3563 & 0.3563 & 2.1779 & 2.1779 & 0.1010 & -0.1010 & -0.3784 & 0.3784 & -0.5549 & -0.9376 & 0
\end{bmatrix}$$

(a)

$$\mathbf{M} = \begin{bmatrix}
0 & -0.3563 & -0.3563 & -2.1779 & -2.1779 & 0.1010 & -0.1010 & -0.3784 & 0.3784 & -0.5549 & -0.7841 & -0.5141 & 0 \\
-0.3563 & 0.9721 & 0 & 0 & 0 & 0 & 0 & 0 & 0 & 0 & 0 & 0 & 0.3563 \\
-0.3563 & 0 & -0.9721 & 0 & 0 & 0 & 0 & 0 & 0 & 0 & 0 & 0 & 0.3563 \\
-2.1779 & 0 & 0 & 2.4778 & 0 & 0 & 0 & 0 & 0 & 0 & 0 & 0 & 2.1779 \\
-2.1779 & 0 & 0 & 0 & -2.4778 & 0 & 0 & 0 & 0 & 0 & 0 & 0 & 2.1779 \\
0.1010 & 0 & 0 & 0 & 0 & 0.6908 & 0 & 0 & 0 & 0 & 0 & 0 & 0.1010 \\
-0.1010 & 0 & 0 & 0 & 0 & 0 & -0.6908 & 0 & 0 & 0 & 0 & 0 & -0.1010 \\
-0.3784 & 0 & 0 & 0 & 0 & 0 & 0 & 1.3055 & 0 & 0 & 0 & 0 & -0.3784 \\
0.3784 & 0 & 0 & 0 & 0 & 0 & 0 & 0 & -1.3055 & 0 & 0 & 0 & 0.3784 \\
-0.5549 & 0 & 0 & 0 & 0 & 0 & 0 & 0 & 0 & 0 & 0 & 0 & -0.5549 \\
-0.7841 & 0 & 0 & 0 & 0 & 0 & 0 & 0 & 0 & 0 & 0 & 0 & 0.7841 \\
-0.5141 & 0 & 0 & 0 & 0 & 0 & 0 & 0 & 0 & 0 & 0 & 0 & 0.5141 \\
0 & 0.3563 & 0.3563 & 2.1779 & 2.1779 & 0.1010 & -0.1010 & -0.3784 & 0.3784 & -0.5549 & 0.7841 & 0.5141 & 0
\end{bmatrix}$$

(b)

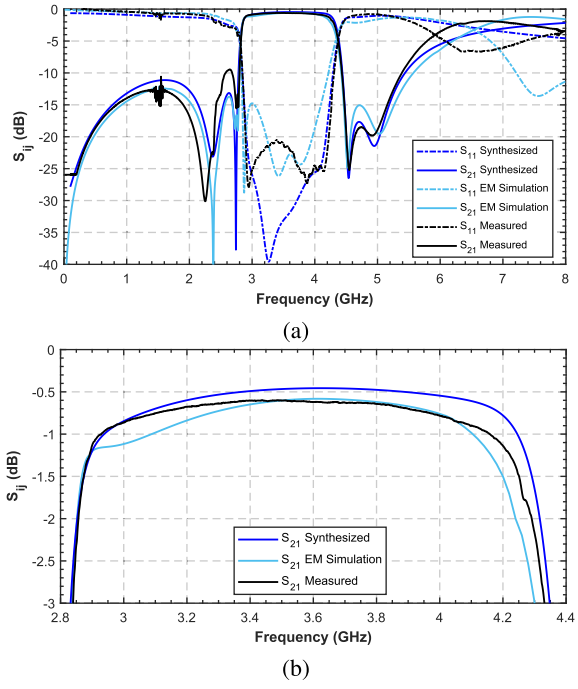
$$\mathbf{M} = \begin{bmatrix}
0 & 1.000 & 0 & 0 & 0 & 1.000 & 0 & 0 & 0 & 0 & 0 & 1.000 & 0 \\
1.000 & 0 & -1.000 & 0 & 0 & 0 & 0 & 0 & 0 & 0 & 0 & 0 & 0 \\
0 & -1.000 & 0 & 1.000 & 0 & 0 & 0 & 0 & 0 & 0 & 0 & 0 & 0 \\
0 & 0 & 1.000 & 0 & 1.000 & 0 & 0 & 0 & 0 & 0 & 0 & 0 & -1.000 \\
0 & 0 & 0 & 1.000 & 0 & 0 & 0 & 0 & 0 & 0 & 0 & 0 & 0 \\
1.000 & 0 & 0 & 0 & 0 & 0 & -1.000 & 0 & 0 & 1.000 & -1.000 & 0 & 0 \\
0 & 0 & 0 & 0 & 0 & -1.000 & 0 & 1.000 & 0 & 0 & 0 & 0 & 0 \\
0 & 0 & 0 & 0 & 0 & 0 & 1.000 & 0 & -1.000 & 0 & 0 & 0 & 0 \\
0 & 0 & 0 & 0 & 0 & 0 & 0 & -1.000 & 0 & 0 & 0 & 0 & 0 \\
0 & 0 & 0 & 0 & 0 & 1.000 & 0 & 0 & 0 & 0 & 0 & 0 & 0 \\
0 & 0 & 0 & 0 & 0 & -1.000 & 0 & 0 & 0 & 0 & 0 & 0 & 1.000 \\
1.000 & 0 & 0 & 0 & 0 & 0 & 0 & 0 & 0 & 0 & 0 & 0 & -1.000 \\
0 & 0 & 0 & -1.000 & 0 & 0 & 0 & 0 & 0 & 0 & 1.000 & -1.000 & 0
\end{bmatrix}$$

(c)

$$\mathbf{W} = \begin{bmatrix}
0 & 0 & 0 & 0 & 0 & 0 & 0 & 0 & 0 & 0 & 0 & 0 & 0 \\
0 & 0.1027 & 0 & 0 & 0 & 0 & 0 & 0 & 0 & 0 & 0 & 0 & 0 \\
0 & 0 & 1.6223 & 0 & 0 & 0 & 0 & 0 & 0 & 0 & 0 & 0 & -1.6223 \\
0 & 0 & 0 & 5.4024 & 0 & 0 & 0 & 0 & 0 & 0 & 0 & 0 & 0 \\
0 & 0 & 0 & 0 & 0.1916 & 0 & 0 & 0 & 0 & 0 & 0 & 0 & 0 \\
0 & 0 & 0 & 0 & 0 & 0.8133 & 0 & 0 & 0 & 0 & 0 & 0 & 0 \\
0 & 0 & 0 & 0 & 0 & 0 & 3.0360 & 0 & 0 & 0 & 0 & 0 & 0 \\
0 & 0 & 0 & 0 & 0 & 0 & 0 & 5.7161 & 0 & 0 & 0 & 0 & 0 \\
0 & 0 & 0 & 0 & 0 & 0 & 0 & 0 & 0.3491 & 0 & 0 & 0 & 0 \\
0 & 0 & 0 & 0 & 0 & 0 & 0 & 0 & 0 & 0.4053 & 0 & 0 & 0 \\
0 & 0 & 0 & 0 & 0 & 0 & 0 & 0 & 0 & 0 & 0.8133 & 0 & 0 \\
0 & 0 & 0 & 0 & 0 & 0 & 0 & 0 & 0 & 0 & 0 & 3.7834 & 0 \\
0 & 0 & -1.6223 & 0 & 0 & 0 & 0 & 0 & 0 & 0 & 0 & 0 & 1.6223
\end{bmatrix}$$

(d)

Fig. 18. Matrices corresponding to the BPF 1 of Fig. 2(c): (a) transversal CM before splitting the odd null EV, (b) transversal CM after splitting the odd null EV, (c) final **M**, and (d) final **W**.



(a)

(b)

Fig. 19. BPF 1 filter response: (a) wideband view and (b) in-band view.

the characteristic polynomials are calculated as in [35] to define a dual-band response within $\Omega \in [-1, -f_{c1}/f_{c2}]$ and $\Omega \in [f_{c1}/f_{c2}, 1]$. The corresponding transversal **M** is obtained using (6). Fig. 18(a) shows the transversal CM after expanding the source and load and diagonalizing the CM to increase the

TABLE III

SYNTHESIZED ELEMENTS OF THE BPF 1 AND BPF 2 FILTERS

AW Parameters			
Resonator	C_{stat} **(pF)**	f_s **(MHz)**	k_t^2 **(%)**
BPF 1 (SE)	1.321	4029	12.7
BPF 1 (SH)	2.577	2900	12.4
BPF 2 (SE)	1.639	4029	12.7
BPF 2 (SH)	0.894	2900	12.7
BPF 1 Lumped Elements			
L_{s1} (nH)	1.131	L_{s2} (nH)	1.131
L_p (nH)	0.814	L_b (nH)	0.290
L_g (nH)	0.204		
BPF 2 Lumped Elements			
C_{s1} (pF)	0.857	C_{s2} (pF)	0.857
L_{b1} (nH)	0.752	L_{b2} (nH)	0.752
L_{shu} (nH)	1.017	L_g (nH)	1.830

$$\mathbf{M} = \begin{bmatrix}
0 & 0.3333 & -0.3333 & -0.0841 & -0.0841 & 0.3507 & -0.3507 & -0.5750 & 1.1565 & 0 \\
0.3333 & -0.9662 & 0 & 0 & 0 & 0 & 0 & 0 & 0 & -0.3333 \\
-0.3333 & 0 & 0.9662 & 0 & 0 & 0 & 0 & 0 & 0 & 0.3333 \\
-0.0841 & 0 & 0 & -0.6946 & 0 & 0 & 0 & 0 & 0 & -0.0841 \\
-0.0841 & 0 & 0 & 0 & 0.6946 & 0 & 0 & 0 & 0 & -0.0841 \\
0.3507 & 0 & 0 & 0 & 0 & -1.2403 & 0 & 0 & 0 & 0.3507 \\
-0.3507 & 0 & 0 & 0 & 0 & 0 & 1.2403 & 0 & 0 & -0.3507 \\
-0.5750 & 0 & 0 & 0 & 0 & 0 & 0 & -0.0000 & 0.0000 & -0.5750 \\
1.1565 & 0 & 0 & 0 & 0 & 0 & 0 & 0.0000 & -0.0000 & -1.1565 \\
0 & -0.3333 & 0.3333 & -0.0841 & -0.0841 & 0.3507 & -0.3507 & -0.5750 & -1.1565 & 0
\end{bmatrix}$$

(a)

$$\mathbf{W} = \begin{bmatrix}
2.6136 & 0 & 0 & 0 & 0 & 0 & 0 & 0 & 0 & -2.6136 \\
0 & 1.0000 & 0 & 0 & 0 & 0 & 0 & 0 & 0 & 0 \\
0 & 0 & 1.0000 & 0 & 0 & 0 & 0 & 0 & 0 & 0 \\
0 & 0 & 0 & 1.0000 & 0 & 0 & 0 & 0 & 0 & 0 \\
0 & 0 & 0 & 0 & 1.0000 & 0 & 0 & 0 & 0 & 0 \\
0 & 0 & 0 & 0 & 0 & 1.0000 & 0 & 0 & 0 & 0 \\
0 & 0 & 0 & 0 & 0 & 0 & 1.0000 & 0 & 0 & 0 \\
0 & 0 & 0 & 0 & 0 & 0 & 0 & 1.0000 & -0.0000 & 0 \\
0 & 0 & 0 & 0 & 0 & 0 & 0 & -0.0000 & 1.0000 & 0 \\
-2.6136 & 0 & 0 & 0 & 0 & 0 & 0 & 0 & 0 & 2.6136
\end{bmatrix}$$

(b)

$$\mathbf{M} = \begin{bmatrix}
0 & 1.0000 & 0 & 0 & 0 & 0 & 0 & 1.0000 & 0 & 0 \\
1.0000 & 0 & -1.0000 & 0 & 0 & 0 & 0 & 0 & 0 & -1.0000 \\
0 & -1.0000 & 0 & 0 & 0 & 0 & 0 & 0 & 0 & 0 \\
0 & 0 & 0 & 1.0000 & 0 & 0 & 0 & 0 & 0 & 0 \\
0 & 0 & 0 & 0 & 1.0000 & 0 & 0 & 0 & 0 & 0 \\
0 & 0 & 0 & 0 & 0 & 1.0000 & 0 & 0 & 0 & 0 \\
0 & 0 & 0 & 0 & 0 & 0 & 1.0000 & 0 & 0 & 0 \\
1.0000 & 0 & 0 & 0 & 0 & 0 & 0 & 0 & 0 & 0 \\
0 & 0 & 0 & 0 & 0 & 0 & 0 & 0 & 0 & -1.0000 \\
0 & -1.0000 & 0 & 0 & 0 & 0 & 0 & 0 & -1.0000 & 0
\end{bmatrix}$$

(c)

$$\mathbf{W} = \begin{bmatrix}
2.8028 & 0 & 0 & 0.3785 & 0 & 0 & 0 & 0 & 0 & -2.4243 \\
0 & 4.5005 & 0 & 0 & 0 & 0 & 0 & 0 & 0 & 0 \\
0 & 0 & 0.2380 & 0 & 0 & 0 & 0 & 0 & 0 & 0 \\
0.3785 & 0 & 0 & 0.7570 & 0 & 0 & 0 & 0 & 0 & 0.3785 \\
0 & 0 & 0 & 0 & 0.9609 & 0 & 0 & 0 & 0 & 0 \\
0 & 0 & 0 & 0 & 0 & 9.7983 & 0 & 0 & 0 & 0 \\
0 & 0 & 0 & 0 & 0 & 0 & 0.1891 & 0 & 0 & 0 \\
0 & 0 & 0 & 0 & 0 & 0 & 0 & 0.9431 & -0.5693 & 0 \\
0 & 0 & 0 & 0 & 0 & 0 & 0 & -0.5693 & 0.9431 & 0 \\
-2.4243 & 0 & 0 & 0.3785 & 0 & 0 & 0 & 0 & 0 & 2.8028
\end{bmatrix}$$

(d)

Fig. 20. Matrices corresponding to the BPF 2 of Fig. 2(d): (a) transversal **M** after matrix reduction, (b) transversal **W** after matrix reduction, (c) final **M**, and (d) final **W**.

number of reactive nodes to 10. To prevent the appearance of the undesired cross-coupling, the null odd EV is split using (15) and (16), leading to the equivalent transversal CM shown in Fig. 18(b), which contains 11 reactive nodes. Then, the set of transformations summarized in Fig. 14 is applied, and all entries of **M** are scaled to 1, allowing the elements to be obtained directly from the nodal positions in **W**. The resulting **M** and **W** matrices are presented in Fig. 18(c) and (d), respectively. Table III lists the extracted elements from **W** after scaling them to the upper cutoff frequency. The resulting BPF response is shown in Fig. 19.

In the case of the BPF 2, a ninth-order filter with $\Omega_{TZ} = [\pm 0.614, \pm 1.062, 0.679, 1.165]$ rad/s, and $RL = 27.59$ dB is

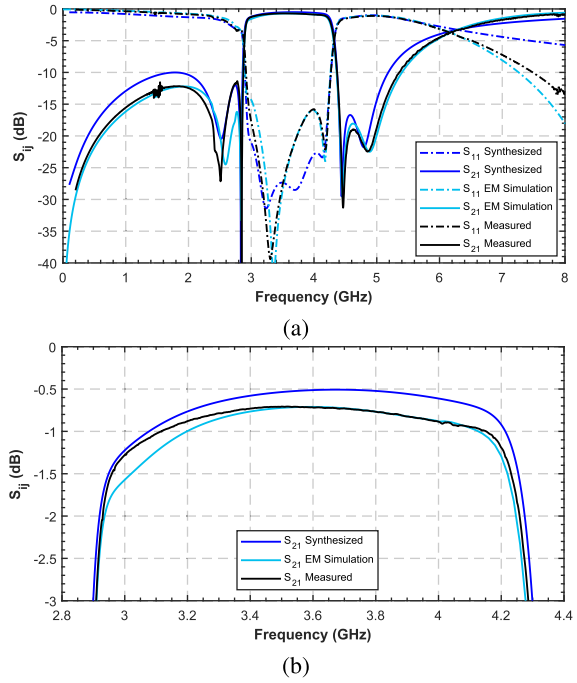


Fig. 21. BPF 2 filter response: (a) wideband view and (b) in-band view.

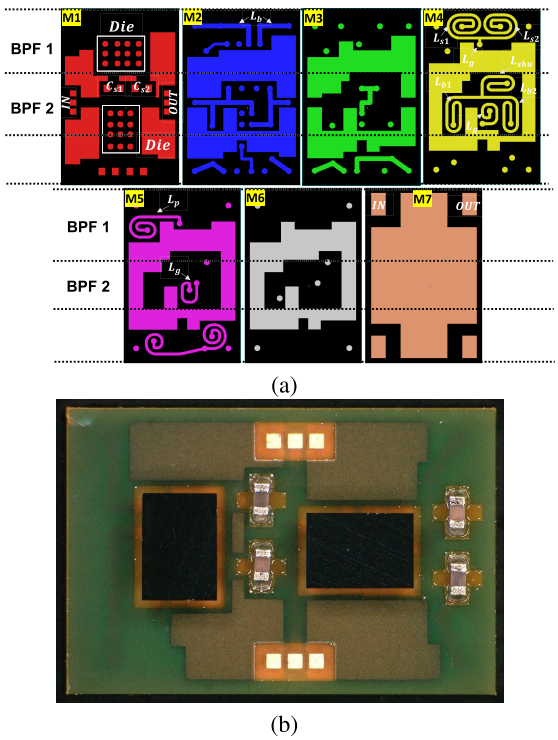


Fig. 22. 3 × 2 mm laminate containing the BPFs: (a) 2-D design view and (b) top-view picture of the assembled design after flipping and mounting the dies.

selected. Considering that $f_{c1} = 2.95$ GHz and $f_{c2} = 4.17$ GHz, the characteristic polynomials are calculated as in [35] to define a dual-band response within $\Omega \in [-1, -f_{c1}/f_{c2}]$ and $\Omega \in [f_{c1}/f_{c2}, 1]$. After calculating the characteristic polynomials, the corresponding transversal $\mathbf{M}$ is obtained with (6). Fig. 20(a) and (b) illustrates the $\mathbf{M}$ and $\mathbf{W}$ matrices, respectively, once the matrix reduction operation is carried out. Then, the set of transformations summarized in Fig. 17 is applied, and expressions (20) and (20) are used to obtain evenly-distributed k_t^2 for both AW resonators. After that, all entries of $\mathbf{M}$ are scaled to 1, allowing the elements to be obtained directly from the nodal positions in $\mathbf{W}$. The resulting $\mathbf{M}$ and $\mathbf{W}$ matrices are presented in Fig. 20(c) and (d), respectively. Table III lists the extracted elements from $\mathbf{W}$ after scaling them to the upper cutoff frequency (4.17 GHz). The resulting BPF response is depicted in Fig. 21.

Table III is used as a reference for designing the BAW resonators. The remaining $f_s = 4030$ MHz is used for series BPF resonators, whereas the $f_s = 2900$ MHz is used for shunt resonators. In this case, the border ring technique is used only for BPF shunt resonators and is avoided for series BPF resonators. The remaining elements of both BPFs are implemented in a different seven-layer laminate. Similar to the LPF and HPF BAW-assisted design, the flipped dies, together with the SMD capacitors C_{s1} and C_{s2} of BPF 2, are placed on the top layer of the laminate. The intermediate layers contain the remaining inductors L_{s1}, L_{s2}, L_b, L_p, and L_g of BPF 1 and L_{b1}, L_{b2}, L_{shunt}, and L_g of BPF 2. The laminate design is shown in Fig. 22(a), where BPF 1 is located at the top, BPF 2 in the middle, and another BT topology that is not explained in this work at the bottom.

Fig. 22(b) shows a top-view picture of the assembled design. BPF 1 is measured using an EVB, whereas BPF 2 is measured with GSG probes. Figs. 19 and 21 compare the synthesized, simulated, and measured S-parameters of BPF 1 and BPF 2, respectively. Both BPFs exhibit a fabricated response with lower insertion loss than the EM-simulated one. This behavior can be partly attributed to a degradation in selectivity caused by manufacturing tolerances, although inaccuracies in the EM models may also contribute to the observed discrepancies.

V. Strategies for Improving OoB Rejection

From a synthesis perspective, the design of two or more cascaded networks can be carried out in two different ways. The first approach, here referred to as *cascading*, consists of defining the filtering function of each network independently, such that the output impedance of one network is the complex conjugate of the input impedance of the other. The second approach, referred to as *decomposition* [24], consists of defining an overall filtering function that accounts for all networks simultaneously. Using the CM approach, the decomposition strategy becomes possible, providing an optimal equiripple response and improved OoB rejection compared with the cascade approach.

Nevertheless, thanks to the properties of the CM, it is straightforward to observe that the LPF and HPF shown in Figs. 3 and 4 require additional shunt capacitors at both the input and output when the network is asymmetrized. This information is very important, because in the decomposition approach, individual cells must become asymmetric so that each section provides the conjugate match of the other. However, in BT topologies, this comes at a cost: Fig. 23 shows that, for a single LPF synthesized with different

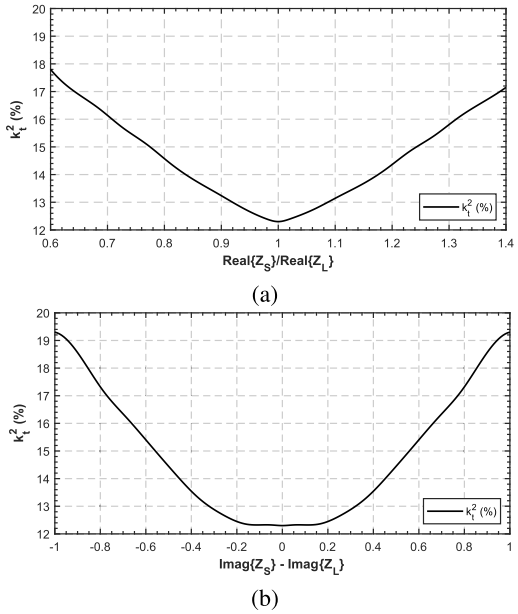


Fig. 23. Impact of source and load impedance asymmetry on the shunt resonator of the LPF: (a) sweep of the real part of Z_L while keeping the normalized source impedance at $Z_S = 1\Omega$ and (b) sweep of the imaginary part of Z_L while keeping the normalized source impedance at $Z_S = 1\Omega$.

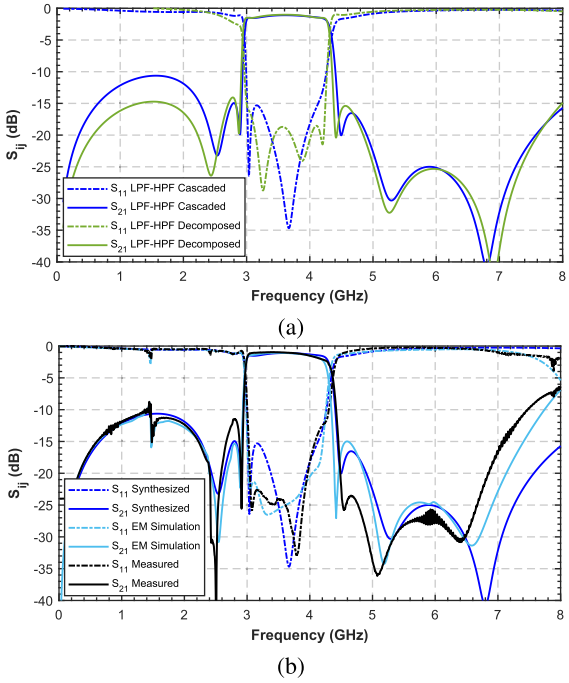


Fig. 24. LPF–HPF filter response: (a) comparison between the cascaded and decomposed designs and (b) comparison of the cascaded design with the EM simulation and the fabricated prototype.

source and load impedances, the minimum k_t^2 is achieved when the BT cell remains symmetric and does not include C_{in} and C_{out}. This is because, in symmetric configurations, C_{in} and C_{out} are absorbed into the shunt resonator, increasing its static capacitance and, consequently, minimizing the required k_t^2.

Interestingly, when the LPF and HPF sections are combined using either the cascade approach or the decomposition approach, both designs tend to converge toward nearly the same solution, as shown in Fig. 24(a) and Table IV. Although the decomposed design provides a slightly improved filter response, its performance remains very close to that of the cascaded design. This behavior is explained by the aforementioned k_t^2 constraint, which limits the advantages of the decomposition approach and drives the solution toward symmetric cells with minimum k_t^2. As a result, BT filter designs with shunt AW resonators tend to converge toward symmetric configurations when the k_t^2 is fixed.

Since the cascaded and decomposition-based approaches provide nearly identical responses, the cascaded implementation is chosen to minimize fabrication complexity. Fig. 24(b) compares the synthesized, simulated, and measured S-parameters of the resulting low-pass and high-pass filter design. Notice how the OoB rejection is better than that of the BPFs. However, its insertion loss is higher than that of the individual cells, because each BT cell introduces, on average, approximately 0.5 dB of additional loss. The presented combination represents only one possible implementation, and many alternative configurations may provide even better performance. For this reason, the synthesis tools presented in this work become valuable, as they enable the systematic evaluation of multiple topological combinations, including ladder networks, until the most suitable broadband solution is identified.

TABLE IV

EXTRACTED ELEMENTS FOR THE CASCADED AND DECOMPOSES LPF–HPF DESIGNS

Element	Decomposed Case		Cascaded Case	
	LPF	HPF	LPF	HPF
C_{stat} (pF)	0.769	0.288	1.200	0.476
f_s (MHz)	4261	2900	4261	2900
k_t^2 (%)	12.4	12.7	12.4	12.7
C_{in} (pF)	0.227	No	No	No
C_{out} (pF)	No	No	No	No
C_{s1} (pF)	1.936	0.361	1.905	0.394
C_{s2} (pF)	1.402	0.343	1.905	0.394
L_b (nH)	1.443	—	1.327	—
L_g (nH)	0.695	—	0.436	—
L_{shu} (nH)	—	4.038	—	3.787

TABLE V

BENCHMARKING AGAINST OTHER LARGE FBW FILTERS

Ref.	FBW (%) @3dB	k_t^2 (%)	IL_{min} (dB)	OoB (dB)	size (mm^2)	Technology
[14]	24	13	0.65	15	0.4×0.55	AlScN/BAW
[36]	24.2	14	2	28	1×0.85	AlScN BAW+IPD
[37]	24.17	N/A	1.16	15	1.57×1.27	IPD
[38]	24	N/A	2.7	25	2×1.25	IPD
[39]	16	25.6	0.7	17.8	?	LN/SiC SAW
[40]	15.6	19.9	1.24	28.1	1.1×1.1	LN/SiC SAW
[40]	24.8	24.4	1.53	18.7	1.1×1.1	LN/SiC SAW
[41]	19.6	24.1	1.27	30	?	LN/SiO_2 SAW
[41]	29.4	24.1	0.73	7.3	?	LN/SiO_2 SAW
This work (BPF 1)	39.31	12.5	0.65	13	3×2	AlScN BAW+PCB
This work (BPF 2)	39	12.5	0.7	12	3×2	AlScN BAW+PCB
This work (LPF+HPF)	36.87	12.5	0.95	12	3×2	AlScN BAW+PCB

VI. Results Discussion

Table V highlights the differences and improvements in key parameters, such as FBW, k_t^2, insertion loss, and OoB rejection, compared with other broadband filters based on miniaturized technologies reported in the IEEE literature. In [14], a comparable performance is achieved using a transversal filter with a smaller FBW. However, it requires an ideal balun to convert the differential measurement into a single-ended response and compensate for the phase imbalance between the parallel-connected branches. This increases fabrication complexity and may introduce spikes. In [36], a filter combining AlScN BAW resonators with IPD technology is presented, similar to this work. However, it exhibits an insertion loss of around 2 dB at the center of the passband, which further degrades toward the lower band edge. In [37] and [38], purely IPD-based filters can achieve FBWs of up to 24%, but the absence of AW resonators leads to higher insertion losses and poorer selectivity. In [39], [40], and [41], it is shown how SAW filters implemented with LN/SiC or LN/SiO2 can also achieve large FBW. However, it requires high k_t^2 values, which leads to higher insertion loss due to the reduced quality factor.

In contrast, the BAW-assisted filters presented in this work achieve the highest FBW with the lowest k_t^2 value. This allows the use of AW resonators with a higher quality factor, resulting in competitive insertion loss levels of 0.6–0.9 dB at the center frequency. Although the lumped elements exhibit lower Q factors than AW resonators, most of them do not directly participate in the resonance process, so their impact on the filter response remains limited.

Nevertheless, as discussed in Section I, BAW-assisted filters alone cannot provide very strong OoB rejection due to their low effective filter order. We refer to effective order because filter order is commonly understood as the number of resonators, or equivalently the number of in-band reflection zeros, rather than the polynomial order used in the DB formulation. From this perspective, although BPF 1 and BPF 2 are represented as tenth- and ninth-order responses in the DB domain, both are effectively fourth-order filters, as they exhibit four in-band reflection zeros. A conventional fourth-order ladder implementation with an equivalent FBW of 33% would require $k_t^2 > 35\%$ to obtain an equivalent OoB rejection, whereas the proposed BAW-assisted designs operate with $k_t^2 \approx 12.5\%$. While ladder filters are limited in achieving extremely large FBWs, BT topologies alone cannot provide strong OoB rejection. Combining both approaches makes it possible to exploit the strengths of each and realize high-performance broadband filters.

VII. Sensitivity Analysis

Transversal topologies are more sensitive network configurations than ladder topologies and are severely affected by element variations when manufacturing tolerances are taken into account [14], [42]. Although BT networks are not purely transversal topologies, their parallel-connected branches cause a strong dependence between both pairs of arms, making any impedance variation that unbalances the topology critical for the response behavior. As detailed in [43], the sensitivity of

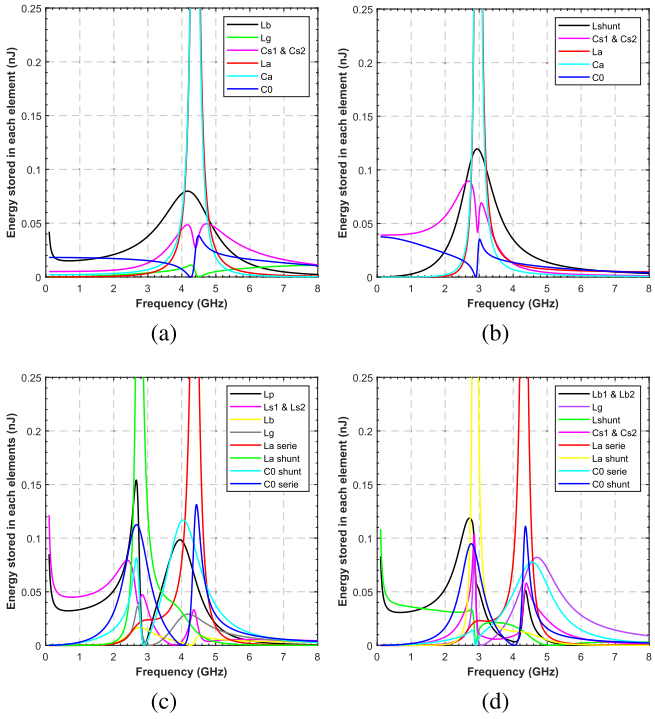


Fig. 25. Energy stored in each of the elements of all BT topologies: (a) LPF, (b) HPF, (c) BPF 1, and (d) BPF 2.

a specific filter topology can be evaluated by studying the components of the gradient of the reflection and transmission coefficients with respect to the entries of the CM. Moreover, in [44] a relationship between the time average stored energy of each CM entry and the sensitivity of the reflection parameter was established, which was used in [45] to improve the yield in specific frequency ranges by optimizing the stored energy in all AW resonators using the TZs and *RL* of the filtering function.

To calculate the energy stored in each element using the proposed CM approach, the BT admittance matrix $\mathbf{Y} = [\mathbf{Z}]^{-1}$ obtained from (1) can be reused after applying each set of transformations to determine the node voltages as follows:

$$\Delta V(\omega) = I_S \cdot \left(\mathbf{Y}_{1,k}(\omega) - \mathbf{Y}_{1,l}(\omega)\right) \cdot Z_0 \tag{22}$$

where ω is the angular frequency, $I_S = (8P_{in} \cdot Z_s)^{1/2}/Z_0$ is the source current, and k and l denote the pair of nodes across each element. If one terminal of the element is connected to ground, the corresponding $\mathbf{Y}_{1,l}(\omega)$ term is taken as zero. Knowing the currents and drop voltages, the stored energies in each capacitor and inductor are calculated as

$$W_C = \frac{1}{4}|\Delta V(\omega)|^2 C \tag{23}$$

$$W_L = \frac{1}{4}|I(\omega)|^2 L. \tag{24}$$

Manufacturing errors in elements with higher stored energy are expected to cause greater variations in the filter response. Assuming an input power of 1 W, Fig. 25 depicts the energy stored for the four BAW-assisted designs.

Fig. 26 presents the sensitivity analysis of the LPF, illustrating the effects of a ±3% variation in the nominal value

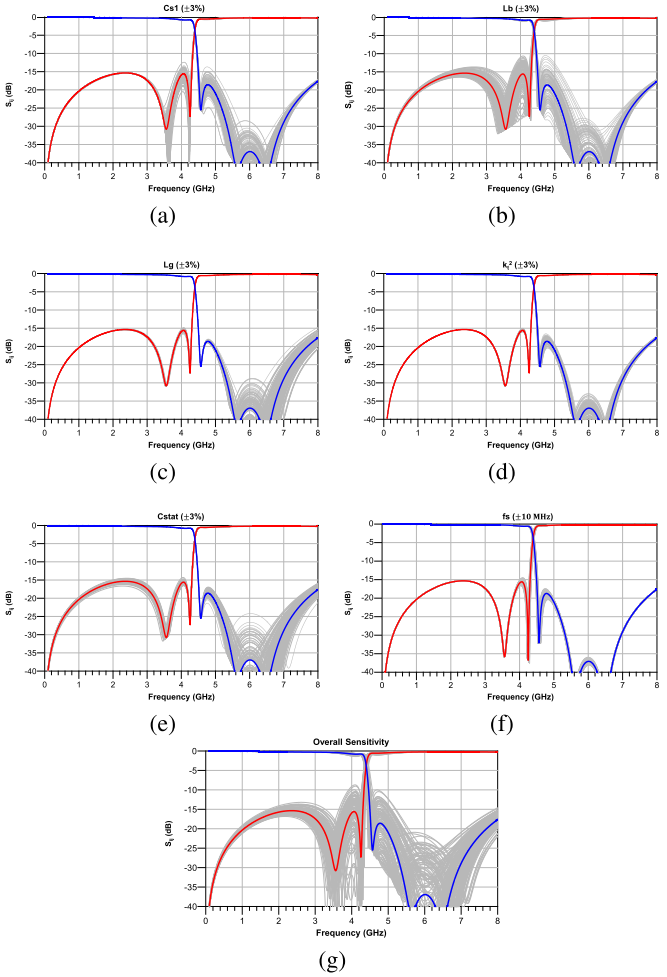


Fig. 26. Sensitivity analysis of the LPF: (a) C_{s1}, (b) L_{b1}, (c) L_g, (d) k_t^2, (e) C_{stat} , (f) f_s, and (g) overall sensitivity.

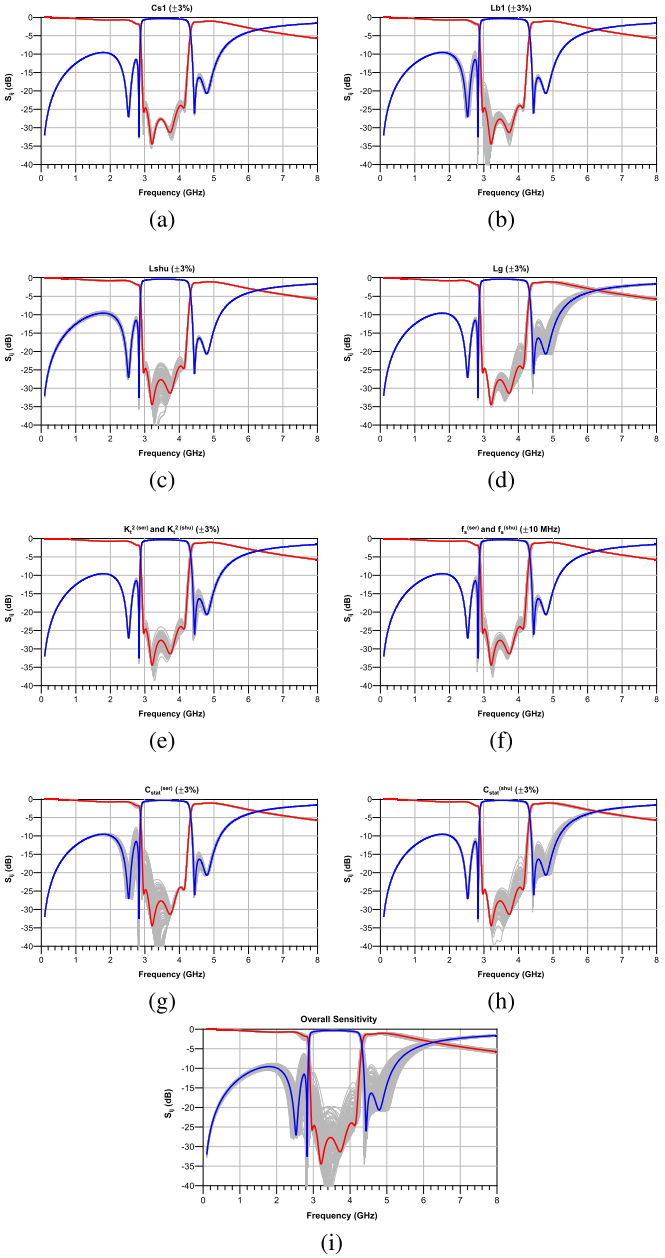


Fig. 27. Sensitivity analysis of the BPF 2: (a) C_{s1}, (b) L_{b1}, (c) L_g, (d) k_t^2, (e) $k_t^{2(ser)}$ and $k_t^{2(shu)}$, (f) $f_s^{(ser)}$ and $f_s^{(shu)}$, (g) C_{stat}^{ser}, (h) C_{stat}^{shu}, and (i) overall sensitivity.

of each element. Let us emphasize that the same variation is assumed for all parameters to enable a fair comparison of their relative sensitivities. The only exception is the f_s, for which a $\pm$10-MHz variation is considered, reflecting the significantly tighter tolerances achievable through high-precision trimming processes.

According to Fig. 26, the most sensitive LPF parameters are L_a and C_a, which determine the f_s of the BVD resonator. This result is expected because the filter response near the band-edge is mainly determined by f_s.

It should be noted, however, that the sensitivity analysis compares the effect of equivalent parameter variations rather than their actual manufacturing spreads. In practice, the variation of f_s after trimming is expected to be considerably smaller than the tolerances of the lumped elements. Therefore, from a manufacturing yield perspective, the parallel-connected inductor L_b becomes the most critical element, as it combines high sensitivity with larger fabrication tolerances than f_s.

Although L_b contributes less energy at the band-edge than L_a and C_a, it contributes more energy across the rest of the frequency spectrum. This explains why the sensitivity analysis of Fig. 26 shows worse performance in those frequency ranges for the L_b case. Similarly, L_g and C_{stat} are the most sensitive elements further from the passband, as they contribute more energy in far-band OoB regions. Fig. 26(g) shows the sensitivity of the LPF when all elements are varied simultaneously.

Since the LPF exhibits a topology very similar to that of BPF 2, the same sensitivity analysis is performed for BPF 2 in Fig. 27. According to Fig. 25(d), series resonators contribute more energy near the upper band edge, whereas the shunt resonators mainly affect the lower band edge. The remaining lumped elements contribute less OoB energy than those in the LPF and HPF. This is because the analyzed BPF circuits consist of three parallel-connected branches instead of two, which distributes the energy across more paths than in the LPF and HPF topologies. As a result, Fig. 27(i) exhibits lower

sensitivity than Fig. 26(g) because the same amount of energy is shared among a larger number of elements.

Regarding the other two BAW-assisted filters, the most sensitive element in the OoB region of the HPF according to Fig. 25(b) is the inductor L_{shunt}. This inductor becomes larger and more sensitive as one of the TZs approaches the passband. On the other hand, the most sensitive elements in the OoB region of BPF 1, according to Fig. 25(c), are L_s andL_p.

VIII. Conclusion

This work explores four BT topologies with strong potential for broadband filtering applications. A CM-based methodology operating in the DB domain is presented, allowing for the automatic extraction of the circuit elements of each BT network. Five proof-of-concept BAW-assisted designs have been implemented to demonstrate that, by using resonators with only $k_t^2 \approx 12.5\%$, it is possible to achieve bandpass filtering responses with an FBW of 33%, something not achievable with conventional ladder networks. Although the use of planar inductors makes the resulting filter area slightly larger than an AW ladder, the BT filter's performance is good enough to assist or even compete with the traditional ladder when the FBW is very large. Since BAW-assisted filters alone cannot achieve very high OoB rejection levels due to their low filter order, they can be used for assisting other networks to achieve better performance at the cost of increased device area and reduced insertion loss. While BAW-assisted filters offer clear advantages over ladder topologies in terms of achievable FBW, they are more sensitive to element variations.

References

[1] A. Hagelauer et al., "From microwave acoustic filters to millimeter-wave operation and new applications," *IEEE J. Microw.*, vol. 3, no. 1, pp. 484–508, Jan. 2023.

[2] A. Hagelauer, G. Fattinger, C. C. W. Ruppel, M. Ueda, K.-Y. Hashimoto, and A. Tag, "Microwave acoustic wave devices: Recent advances on architectures, modeling, materials, and packaging," *IEEE Trans. Microw. Theory Techn.*, vol. 66, no. 10, pp. 4548–4562, Oct. 2018.

[3] A. Giménez, J. Verdú, and P. De Paco Sánchez, "General synthesis methodology for the design of acoustic wave ladder filters and duplexers," *IEEE Access*, vol. 6, pp. 47969–47979, 2018.

[4] P. Warder and A. Link, "Golden age for filter design: Innovative and proven approaches for acoustic filter, duplexer, and multiplexer design," *IEEE Microw. Mag.*, vol. 16, no. 7, pp. 60–72, Aug. 2015.

[5] E. Guerrero, L. Acosta, J. Verdú, and P. de Paco, "Direct synthesis of acoustic wave multiplexers built on fully canonical multiport functions," *IEEE Trans. Microw. Theory Techn.*, vol. 71, no. 4, pp. 1391–1401, Apr. 2023.

[6] R. Ruby, "A snapshot in time: The future in filters for cell phones," *IEEE Microw. Mag.*, vol. 16, no. 7, pp. 46–59, Aug. 2015.

[7] H. Campanella, Y. Qian, C. O. Romero, J. S. Wong, J. Giner, and R. Kumar, "Monolithic multiband MEMS RF front-end module for 5G mobile," *J. Microelectromech. Syst.*, vol. 30, no. 1, pp. 72–80, Feb. 2021.

[8] K. Hashimoto, *RF Bulk Acoustic Wave Filters for Communications*. Norwood, MA, USA: Artech House, 2009.

[9] L. Chen et al., "Scandium-doped aluminum nitride for acoustic wave resonators, filters, and ferroelectric memory applications," *ACS Appl. Electron. Mater.*, vol. 5, no. 2, pp. 612–622, Feb. 2023, doi: 10.1021/acsaelm.2c01409.

[10] A. Tag et al., "Next generation of BAW: The new benchmark for RF acoustic technologies," in *Proc. IEEE Int. Ultrason. Symp.*, Oct. 2022, pp. 1–4.

[11] M. Akiyama, T. Kamohara, K. Kano, A. Teshigahara, Y. Takeuchi, and N. Kawahara, "Enhancement of piezoelectric response in scandium aluminum nitride alloy thin films prepared by dual reactive cosputtering," *Adv. Mater.*, vol. 21, no. 5, pp. 593–596, Feb. 2009.

[12] M. Kadota and S. Tanaka, "Ultra-wideband ladder filter using SH_0 plate wave in thin $LiNbO_3$ plate and its application to tunable filter," *IEEE Trans. Ultrason., Ferroelectr., Freq. Control*, vol. 62, no. 5, pp. 939–946, May 2015.

[13] R. Su et al., "Wideband and low-loss surface acoustic wave filter based on 15° YX-$LiNbO_3$/SiO_2/Si structure," *IEEE Electron Device Lett.*, vol. 42, no. 3, pp. 438–441, Mar. 2021.

[14] J. Mateu et al., "Acoustic wave transversal filter for 5G N77 band," *IEEE Trans. Microw. Theory Techn.*, vol. 69, no. 10, pp. 4476–4488, Oct. 2021.

[15] A. Triano, J. Verdu, and P. de Paco Sanchez, "A general synthesis technique of mixed-topology including parallel-connected structures for fully canonical ladder-type acoustic filters," *IEEE Trans. Microw. Theory Techn.*, vol. 67, no. 12, pp. 5061–5068, Dec. 2019.

[16] Q. Yang, W. Pang, D. Zhang, and H. Zhang, "A wideband bulk acoustic wave filter with modified lattice configuration," in *IEEE MTT-S Int. Microw. Symp. Dig.*, May 2015, pp. 1–4.

[17] S. Cano, L. Acosta, C. Caballero, J. Verdú, and P. de Paco, "Synthesis of wideband filters based on acoustic wave transversal and ladder topologies," in *IEEE MTT-S Int. Microw. Symp. Dig.*, May 2024, pp. 101–104.

[18] S. Cano, C. Caballero, L. Acosta, M. Faura, J. Verdú, and P. de Paco, "Breaking the ladder bandwidth limitation: Synthesis of acoustic wave ladder filters adding parallel connected resonators," in *Proc. IEEE Ultrason., Ferroelectr., Freq. Control Joint Symp. (UFFC-JS)*, Sep. 2024, pp. 1–4.

[19] W. P. Mason, "Electrical wave filters employing quartz crystals as elements," *Bell Syst. Tech. J.*, vol. 13, no. 3, pp. 405–452, Jul. 1934.

[20] W. P. Mason and R. A. Sykes, "Electrical wave filters employing crystals with normal and divided electrodes," *Bell Syst. Tech. J.*, vol. 19, no. 2, pp. 221–248, Apr. 1940.

[21] Y. Yusuf, "*Bridge-T filter*," U.S. Patent Application US 2023/0378936 A1, Nov. 23, 2023.

[22] Y. Yusuf, "*Resonator-assisted LC filter exhibiting high-pass and band-pass behavior*," U.S. Patent US 12,294,354 B2, May. 6, 2025.

[23] S. Cano, C. Caballero, O. Barrera, R. Lu, J. Verdú, and P. de Paco, "General synthesis methodology for acoustic wave ladder filters in the bandpass domain," *IEEE Trans. Microw. Theory Techn.*, vol. 73, no. 10, pp. 7055–7068, Oct. 2025.

[24] S. Cano, J. Verdú, and P. de Paco, "Coupling matrix decomposition of acoustic wave ladder filters in the bandpass domain," *IEEE Trans. Microw. Theory Techn.*, vol. 74, no. 1, pp. 569–580, Jan. 2026.

[25] S. Darlington, "Synthesis of reactance 4-poles which produce prescribed insertion loss characteristics: Including special applications to filter design," *J. Math. Phys.*, vol. 18, nos. 1–4, pp. 257–353, Apr. 1939.

[26] A. Atia, A. Williams, and R. Newcomb, "Narrow-band multiple-coupled cavity synthesis," *IEEE Trans. Circuits Syst.*, vol. CS-21, no. 5, pp. 649–655, Sep. 1974.

[27] R. J. Cameron, *Microwave Filters for Communication Systems*. Hoboken, NJ, USA: Wiley, 2007.

[28] P. Zhao and K. Wu, "Cascading fundamental building blocks with frequency-dependent couplings in microwave filters," *IEEE Trans. Microw. Theory Techn.*, vol. 67, no. 4, pp. 1432–1440, Apr. 2019.

[29] Y. Zeng, Y. Yang, Y. Wu, M. Yu, J. Peng, and D. Liang, "Exploiting redundancy in direct synthesis for inline filters," *IEEE Trans. Microw. Theory Techn.*, vol. 69, no. 10, pp. 4489–4498, Oct. 2021.

[30] J. Kaitila, M. Ylilammi, J. Ella, and R. Aigner, "Spurious resonance free bulk acoustic wave resonators," in *Proc. IEEE Int. Ultrason. Symp.*, vol. 1, Oct. 2003, pp. 84–87.

[31] C. Udaondo, C. Collado, J. Mateu, and R. Aigner, "Analysis of border ring modes on SMR-BAW resonators," in *Proc. IEEE Int. Ultrason. Symp.*, Oct. 2019, pp. 1703–1706.

[32] W. S. Tsai, C. Y. Huang, C. K. Chung, K. H. Yu, and C. F. Lin, "Generational changes of flip chip interconnection technology," in *Proc. 12th Int. Microsystems, Packag., Assem. Circuits Technol. Conf. (IMPACT)*, Oct. 2017, pp. 306–310.

[33] E. M. Davis, W. E. Harding, R. S. Schwartz, and J. J. Corning, "Solid logic technology: Versatile, high-performance microelectronics," *IBM J. Res. Develop.*, vol. 44, no. 1, pp. 56–68, 2000.

[34] S. Cano, M. Faura, L. Garcia, J. Parrón-Granados, and P. de Paco, "Frequency-dependent impedance matching synthesis methodology for filters or matching networks with equiripple responses," *IEEE Trans. Microw. Theory Techn.*, vol. 74, no. 6, pp. 5536–5550, Jun. 2026.

[35] S. Cano et al., "Enhanced modeling of wideband acoustic wave ladder filters," in *Proc. IEEE Int. Ultrason. Symp.*, Sep. 2025, pp. 1–4.

[36] R. Ding et al., "Compact and high steep skirts hybrid heterogeneous integrated N77 full band BAW filter based on band-stop theory," *IEEE Electron Device Lett.*, vol. 45, no. 5, pp. 793–796, May 2024.
[37] M. Park, D. Park, J. Yu, J.-M. Yook, J.-G. Yook, and D. Kim, "Fabrication of an n77 band-pass filter using advanced glass-IPD technology," in *Proc. IEEE Asia–Pacific Microw. Conf. (APMC)*, Nov. 2024, pp. 766–768.
[38] Q. Qin, J. Song, X. Li, D. Wang, and L. Sun, "Miniaturization of 5G N77 bandpass filter with HR-Si IPD technology," in *Proc. IEEE Int. Conf. Integr. Circuits, Technol. Appl. (ICTA)*, Nov. 2020, pp. 116–118.
[39] H. Xu et al., "Low-loss N79 band SAW filter with 16.0% FBW based on 15° Y-X $LiNbO_3$/SiC structure," *IEEE Electron Device Lett.*, vol. 45, no. 7, pp. 1353–1356, Jul. 2024.
[40] H. Xu et al., "SAW filters on $LiNbO_3$/SiC heterostructure for 5G N77 and N78 band applications," *IEEE Trans. Ultrason., Ferroelectr., Freq. Control*, vol. 70, no. 9, pp. 1157–1169, Sep. 2023.
[41] R. Su et al., "Scaling surface acoustic wave filters on LNOI platform for 5G communication," in *IEDM Tech. Dig.*, Dec. 2022, pp. 4.2.1–4.2.4.
[42] J. Mateu, C. Collado, and R. Aigner, "Practical issues on the implementation of acoustic transversal filters," in *Proc. IEEE Int. Ultrason. Symp. (IUS)*, Oct. 2019, pp. 2576–2579.
[43] S. Amari and U. Rosenberg, "On the sensitivity of coupled resonator filters without some direct couplings," *IEEE Trans. Microw. Theory Techn.*, vol. 51, no. 6, pp. 1767–1773, Jun. 2003.
[44] M. Martinez-Mendoza, F. Seyfert, C. Ernst, and A. Alvarez-Melcon, "Formal expression of sensitivity and energy relationship in the context of the coupling matrix," *IEEE Trans. Microw. Theory Techn.*, vol. 60, no. 11, pp. 3369–3375, Nov. 2012.
[45] S. Cano, M. Faura, E. Guerrero, G. Piris, J. Verdú, and P. de Paco, "Management of stored energy in acoustic wave ladder filters to improve yield," in *Proc. IEEE Int. Microw. Filter Workshop (IMFW)*, Feb. 2024, pp. 136–139.



Santi Cano (Member, IEEE) was born in Sabadell, Spain, in 2000. He received the B.Sc. and M.Sc. degrees in telecommunications engineering from the Universitat Autònoma de Barcelona (UAB) in 2021 and 2023, respectively, where he pursued his Ph.D. degree in electronic and telecommunications engineering.

In 2023, he joined the WavesLab research group at UAB. His doctoral research focused on direct bandpass synthesis techniques for wideband hybrid acoustic wave (AW) filters based on ladder and mixed topologies. During his Ph.D., he participated in the design, fabrication and measurement of BAW (Bulk Acoustic Wave) ladder and BAW-assisted filters, and contributed to the design surface acoustic wave (SAW) ladder filters on Lithium Niobate-on-Insulator. In 2026, he joined the BAW Research and Development group at Qorvo Inc., Barcelona, where he currently works on the technological development of next-generation BAW devices. His main research interests include microwave filter synthesis, acoustic device physics, piezoelectric materials, and BAW and SAW filters for wireless communication applications.



Eloi Guerrero (Member, IEEE) was born in Terrassa, Spain, in 1996. He received the M.Sc. degree (Hons.) and the Ph.D. (cum laude) degrees in telecommunications engineering from the WavesLab Research Group, Universitat Autónoma de Barcelona (UAB), Barcelona, Spain, in 2020 and 2023, respectively, under the supervision of Prof. Pedro de Paco.

Since 2023, he has been with the BAW Research and Development Group, Qorvo Inc., Barcelona, and his main research interests include microwave filter synthesis techniques, BAW and SAW resonators and filters, acoustic device physics, and piezoelectric materials.



Alfred Giménez was born in Lleida, Spain, in 1988. He received the M.S. degree in electrical engineering and the Ph.D. degree (cum laude) from the Universitat Autónoma de Barcelona (UAB), Barcelona, Spain, in 2013 and 2016, respectively. His thesis concerned the development of synthesis methodologies for filters and multiplexer designs based on bulk acoustic wave (BAW) devices.

In 2012, he joined the Antenna and Microwave System Group, UAB, where he was involved in research projects including computer-aided design of microwave filters with BAW and surface acoustic wave (SAW) devices. In 2016, he joined the BAW Research and Development Group, Qorvo Inc., Apopka, FL, USA, where he is currently involved in the technology development of new-generation RF acoustic wave devices. During his career at Qorvo, he has also been involved in various commercial RF modules using BAW filters. His current research interests include the design and synthesis of RF filters and multiplexers, BAW, and SAW devices, and electrical design automation.



Lluis Acosta was born in Terrassa, Spain, in 1996. He received the M.S. degree (Hons.) in electrical engineering and the Ph.D. degree (cum laude) from the Universitat Autónoma de Barcelona (UAB), Barcelona, Spain, in 2021 and 2024, respectively. His Ph.D. thesis focused on the development of synthesis methodologies for filters and multiplexers based on acoustic wave (AW) devices.

In 2020, he joined the WavesLab Research Group, UAB, where he modeled and designed piezoelectric-on-insulator SAW resonators. In 2024, he joined the BAW Research and Development Group, Qorvo Inc., Barcelona, where he is currently involved in the technology development of new-generation RF BAW devices. His current research interests include the synthesis and design of RF filters and multiplexers, BAW, and SAW devices, and electrical design automation.



Carlos Caballero (Associate Member, IEEE) was born in Santa Coloma de Gramenet, Spain, in 1997. He received the B.S. degree (Hons.) and the M.S. degree in telecommunications engineering from the Universitat Autónoma de Barcelona (UAB), Barcelona, Spain, in 2019 and 2022, respectively, where he is currently pursuing the Ph.D. degree at the WavesLab Research Group.

His main research interests include the synthesis of microwave filters and the synthesis and design of microwave acoustic filters.



Yazid Yusuf received the B.S. degree in electrical engineering from Jordan University of Science and Technology, Irbid, Jordan, in 2005, and the M.S. and Ph.D. degrees in electrical engineering and computer science from the University of Central Florida, Orlando, FL, USA, in 2008 and 2011, respectively.

He was a Post-Doctoral Researcher with the University of Wisconsin–Madison, Madison, WI, USA, before joining Qorvo (formerly TriQuint Semiconductor) in 2012. He is currently an Engineering Fellow at the Bulk Acoustic Wave (BAW) Research and Development Group. His work focuses on the physical modeling, analysis, and design of acoustic resonators and RF filters for wireless communication systems. He has authored and co-authored numerous technical publications and holds multiple U.S. patents in RF acoustic devices and filter technologies. His research interests include bulk acoustic wave devices, piezoelectric resonators, acoustic and electromagnetic modeling, and the development of advanced RF filter and multiplexer architectures.



Jordi Verdú (Senior Member, IEEE) was born in Sabadell, Spain. He received the M.S. degree in telecommunication engineering and the Ph.D. degree (cum laude) from the Universitat Autónoma de Barcelona (UAB), Barcelona, Spain, in 2006 and 2010, respectively.

From 2006 to 2010, he was a member of the WavesLab Research Group, UAB. In 2010, he joined the RF System Group, European Spallation Source in Bilbao (ESS-B), as a Group Coordinator. From 2011 to 2012, he was at the École Polytechnique Fédérale de Lausanne, Lausanne, Switzerland, through a Marie Curie grant. In 2013, he joined the Theory Signal Communication Group, Universitat Politécnica de Catalunya, Barcelona. He is currently an Associate Professor at UAB, where he teaches microwave engineering courses. He has been extensively working on linear modeling of acoustic wave devices and new synthesis techniques and advanced configurations for acoustic wave filters. His current research interests include the design of microwave devices and linear modeling, but also the design of active devices for space applications.

Dr. Verdú received the Department Best Thesis Prize for his Ph.D. degree. He is the Vice-Chair of the MTT-6 MEMS and Microwave Acoustics Technical Committee.



Pedro de Paco (Senior Member, IEEE) was born in Badalona, Spain. He received the M.S. degree in telecommunication engineering and the Ph.D. degree (cum laude) from the Universitat Politécnica de Catalunya (UPC), Barcelona, in 1997 and 2003, respectively.

In 1998, he joined the Electromagnetic and Photonics Engineering Group (EEF), Signal Theory and Communications Department (TSC), UPC, with a grant from the Institut d'Estudis Espacials de Catalunya (IEEC) in a joint activity related to European scientific space mission Planck. He was a member of the LFI-Radiometer Working Group and the Planck Consortium. During his Ph.D. degree at UPC stage, he has participated in several national and international research projects mostly related to microwave and millimeter-wave circuits and systems applied to the design and testing of remote sensing instruments and front-end-to-multipoint broadband communication systems. Since 2004, he has been an Associate Professor with the Universitat Autónoma de Barcelona, Barcelona, where he teaches applied electromagnetics and microwave engineering courses. He has advised eight Ph.D. students. From 2010 to 2013, he was the Deputy Director and a member of the Executive Board at the Telecommunication and System Engineering Department, UAB. From 2018 to 2019, he was a Visiting Researcher with the Microwave and RF Research Group, University of Colorado at Boulder, Boulder, CO, USA. His main research interests include microwave filter synthesis and microwave acoustics filter synthesis and design, as well as microwave and radar systems and devices.

Dr. de Paco is a member of the MTT-6 RF MEMS and Microwave Acoustics Committee and a reviewer of IEEE TRANSACTIONS ON MICROWAVE THEORY AND TECHNIQUES and IEEE MICROWAVE AND WIRELESS TECHNOLOGY LETTERS. He serves as a member for the Technical Review Board for European Microwave Conference. He has been appointed as a Technical Expert for Telecommunications Equipment by the National Agency of Accreditation. He was awarded three times for merits in research and recognized with merits in University training by l'Agéncia de Qualitat, and Advanced Research by Generalitat de Catalunya.